Statistics of convective cloud turbulence from a comprehensive turbulence retrieval method for radar observations

Article

Accepted Version

Statistics of Convective Cloud Turbulence from a Comprehensive Turbulence Retrieval Method for Radar Observations

Matthew M. Feist[a*], Chris D. Westbrook[a], Peter A. Clark[a], Thorwald HM. Stein[a], Humphrey W. Lean[b], Alison J. Stirling[c]

[a]*Department of Meteorology, University of Reading, Reading, UK.*

[b]*MetOffice@Reading, University of Reading, Reading, UK.*

[c]*Met Office, Exeter, UK.*

[*]*Correspondence to: M. M. Feist, Department of Meteorology, University of Reading, Reading, RG6 6BB, UK. E-mail: M.M.Feist@pgr.reading.ac.uk*

Turbulent mixing processes are important in determining the evolution of convective clouds, and the production of convective precipitation. However, the exact nature of these impacts remains uncertain due to limited observations. Model simulations show that assumptions made in parametrising turbulence can have a marked effect on the characteristics of simulated clouds. This leads to significant uncertainty in forecasts from convection-permitting numerical weather prediction (NWP) models. This contribution presents a comprehensive method to retrieve turbulence using Doppler weather radar to investigate turbulence in observed clouds. This method involves isolating the turbulent component of the Doppler velocity spectrum width, expressing turbulence intensity as an eddy dissipation rate, ε. By applying this method throughout large datasets of observations collected over the southern UK using the (0.28° beam-width) Chilbolton Advanced Meteorological Radar (CAMRa), statistics of convective

cloud turbulence are presented. Two contrasting case days are examined: a shallow "shower" case, and a "deep convection" case, exhibiting stronger and deeper updrafts. In our observations, ε generally ranges from $10^{-3} - 10^{-1}$ $m^2 s^{-3}$, with the largest values found within, around and above convective updrafts. Vertical profiles of ε suggest that turbulence is much stronger in deep convection; 95th percentile values increase with height from 0.03 – 0.1 $m^2 s^{-3}$, compared to approximately constant values of 0.02 – 0.03 $m^2 s^{-3}$ throughout the depth of shower cloud. In updraft regions on both days, the 95th percentile of ε has significant ($p < 10^{-3}$) positive correlations with the updraft velocity, and the horizontal shear in the updraft velocity, with weaker positive correlations with updraft dimensions. The ε-retrieval method presented considers a very broad range of conditions, providing a reliable framework for turbulence retrieval using high-resolution Doppler weather radar. In applying this method across many observations, the derived turbulence statistics will form the basis for evaluating the parametrisation of turbulence in NWP models.

Keywords: Radar; Doppler spectrum width; turbulence; convection; eddy dissipation rate; clouds.

1 Introduction

The effects of turbulence on the structure and evolution of convective clouds remain unclear in observations and numerical weather prediction (NWP) models. The turbulent entrainment of dry environmental air into cumulus clouds has long been known to play an important role in their growth and decay (Blyth, 1993). The specific location of entrained air can have a varied and substantial impact on resulting air motions within the cloud (Blyth *et al*., 1988). Turbulent mixing within clouds significantly impacts the microphysical processes governing the initiation of convective precipitation; the presence of turbulence accelerates cloud drop growth through increased rates of collision and coalescence (Grover and Pruppacher, 1985; Khain and Pinsky, 1995; Vohl *et al*., 1999;

Falkovic *et al*., 2002; Pinksy and Khain, 2002). Although there is much evidence for the effects of turbulence on cloud processes, there remains uncertainty in their precise nature, and the implications for cloud evolution.

In recent years, regional numerical weather prediction (NWP) has improved to sufficient resolution that it is worthwhile abandoning the parametrisation of deep convective clouds, and, instead, allowing the unstable growth of explicit convective clouds. However, it is not feasible to forecast using resolutions sufficient to properly resolve all of the important features of the flow. Hence such models are known as 'convection-permitting models' (CPMs, Clark *et al*., 2016). Physical processes occurring on scales below those resolved in CPMs, such as turbulence, remain parametrised. CPMs generally adopt mixing-length-based turbulence closure schemes from Large-Eddy Simulation (LES) models, such as the Smagorinsky-Lilly sub-grid scheme. It is not often clear whether the assumptions implicit in these schemes (such as the ability of the model to resolve an inertial sub-range of turbulence) are valid for CPMs, especially when using grid-lengths larger than 100 m. Model simulations show that the configuration of turbulence parametrisations can have a profound effect on the characteristics of simulated clouds (e.g. Hanley *et al*., 2015). Until we advance our understanding of the effects of turbulence in observed clouds, justifiable attempts to evaluate and improve these parametrisations are difficult to make.

To improve our understanding of turbulence in observed clouds for model evaluation, observations of convective storm turbulence can be made with Doppler weather radar. By isolating the turbulent component to the Doppler velocity spectrum variance, near-instantaneous observations of turbulence can be made across large swathes of atmosphere. Turbulence retrieval with weather radar has clear benefits over using methods such as aircraft or ascent measurements which can only collect time-series information from single points in space. Radar retrieved fields of turbulence, expressed for convenience in terms of the dissipation rate of turbulent kinetic energy, ε, can be used to investigate relationships with storm strength and structure in a statistical sense for model evaluation.

The accuracy to which ε can be derived using the Doppler variance method is dependent on the accurate removal of variances associated with processes aside from inertial sub-range turbulence. Due to this somewhat indirect approach, evaluation of the Doppler variance method has previously been necessary through comparison of ε estimates with in situ measurements and other radar retrieval techniques. Using Doppler weather radar, Labitt (1981) and Meischner *et al.* (2001) demonstrated good agreement between ε derived from the Doppler variance method when compared with co-ordinated aircraft measurements in convective storms. Brewster and Zrnic (1986) found a high level of agreement between ε from Doppler variance and ε estimated from the "spatial spectra" method – a method which involves taking the Fourier transform of a dataset of Doppler velocity measurements sampled either along a single ray at a given time, or at a fixed range gate over a period of time. Bouniol *et al.* (2003) performed a similar evaluation of the Doppler variance method using the spatial spectra method with a vertically-pointing Doppler cloud radar. Point-for-point comparison of ε from the two methods showed a high level of agreement, especially for larger values. They concluded that the Doppler variance provides a reliable estimate of ε. The spatial spectra method itself has been evaluated by Shupe *et al.* (2012), who analysed Doppler velocity time series sampled with a vertically-pointing cloud radar in stratocumulus clouds. They found ε estimates from spatial spectra to correspond well with aircraft and sonic anemometer measurements. Albrecht *et al.* (2016) examined cloud-top entrainment processes in non-precipitating stratocumulus using vertically-pointing Doppler cloud radar. In this study, estimates of ε were derived using both the Doppler spectrum variance and the Doppler velocity power spectrum (Fang *et al.*, 2014), with good agreement found between the two methods. Methods to retrieve ε at vertical incidence in (precipitating and non-precipitating) stratocumulus using Doppler cloud radar are not well suited to retrieve ε with scanning Doppler weather radar in precipitating convective clouds; as pertains to this study.

For scanning Doppler weather radar, the most significant contributor to Doppler variance aside from turbulence is generally shear of the radial wind across the three dimensions of the beam (see Section 5), which requires careful separation from turbulence before estimates of ε can be made.

Melnikov and Doviak (2009) present a detailed method to retrieve ε from the Doppler spectrum in vertical cross-sections through stratiform precipitation collected using an S-band Doppler weather radar. In their study, the radial and elevation shear components are calculated by least-squares fitting contiguous Doppler velocity measurements separately in each direction. A similar, though more sophisticated technique is applied in Section 5.3 to use linear regression to fit a 2-D linear velocity surface model (Neter and Wasserman, 1974) to Doppler velocities to evaluate shear over a spatial scale that we can specify and fix, guided by estimates of the inertial sub-range outer-scale (see Section 5.2). Using this method, we have been able to test the sensitivity of retrieved ε to the scale over which shear is calculated and removed (Section 5.5).

Melnikov and Doviak (2009) calculated the azimuthal (transverse) shear from velocity gradients between two adjacent scans separated by 2°. They found variances from azimuthal shear to be small compared to elevation shears in stratiform clouds. However, stronger horizontal shears are likely to be found in the convective clouds analysed in this application; in particular, along the edges of updrafts (e.g. Istok and Doviak, 1986). In the present application, our radar data includes one scan performed through one azimuth per cloud. Consequently, we have developed new methods to estimate the azimuthal shear component from the radial shear alone (Section 5.4), allowing for its variance contribution to be estimated when adjacent scans are not available.

Generally, past studies focus on single storm cases when using radar methods to investigate convective storm turbulence (e.g. Brewster and Zrnic, 1986; Istok and Doviak, 1986). Often, the contributions to the Doppler spectrum width from mechanisms aside from turbulence are either purely assumed to be negligible, or are shown to be negligible only for the purpose of the application. As a result, a comprehensive method to retrieve ε from radar fields under a wide range of conditions, and the statistical assessment of ε that such a method permits, have not been presented. In developing this comprehensive approach, comparison is made with the more limited approaches that have appeared in the literature.

In Sections 2 – 5 of this paper, we present methods to accurately determine ε from radar fields. This includes a summary of the conditions under which certain terms in the Doppler spectrum width equation can be neglected, and detailed methods for their calculation when they cannot. By applying this method across a dataset of radar observations, we have performed a statistical assessment of ε in convective storms; this is presented in Section 6.

2 Data and Methods

2.1 DYMECS – Radar observations with CAMRa

This investigation follows on from the Dynamical and Microphysical Evolution of Convective Storms (DYMECS) project (Stein *et al*., 2014). The primary objective of DYMECS is to apply a statistical approach to investigate the dynamics, morphology and evolution of convective storms over southern England, both in radar observations and in high-resolution Met Office Unified Model (MetUM) simulations. An innovative track-and-scan method was used to obtain radar observations of hundreds of convective storms in 2011-2012. These were collected using the Chilbolton Advanced Meteorological Radar (CAMRa) located at the Chilbolton Observatory in Hampshire, UK. CAMRa is a 3 GHz (S-band) Doppler weather radar with dual-polarisation capability. The 25-m diameter antenna provides an angular beam-width of 0.28°. The narrow beam provides elevation, θ and azimuthal, φ resolutions of 100 m at 20 km range, and 500 m at 100 km range. In the radial direction, the pulse has a length of 75 m, however, this is averaged to 300 m in our observations.

Observations were collected by scanning with CAMRa in two modes: elevation scanning with RHIs (range-height indicator) and azimuthal scanning with PPIs (plan-position indicator). By alternating between these two modes, detailed observations of hundreds of convective storms were collected on 40 days between July 2011 and August 2012. These observations have been compared

with MetUM simulations to characterise storm morphology (Stein *et al*., 2014) and convective updraft characteristics (Nicol *et al*., 2015) in model and observations.

In Section 6, turbulence retrievals are analysed with corresponding fields of vertical velocity retrieved by Nicol *et al*. (2015) for DYMECS observations made on 20 April 2012 and 25 August 2012. These updraft velocities were estimated from the Doppler velocity by vertically integrating local changes in horizontal convergence under the assumption of flow continuity, accounting for the changes in density with height. The use of horizontal convergence to estimate vertical velocity removes the need to consider corrections for hydrometeor fall-speeds. The method required a zero-velocity boundary condition, either at the surface or cloud echo top. A weighted combination of velocity derived under both conditions was developed to minimise the vertical propagation of errors. In using only single-Doppler measurements, the omission of convergence in the direction perpendicular to the scanning plane led to a consistent under-estimation of the vertical velocity. To correct for this under-estimation, the suitable scaling for the vertical velocity was estimated from 500-m grid-length simulations of the MetUM for each case. These were made under assumptions that the simulated three-dimensional wind flows were suitably realistic and that the range of observed vertical velocities was represented in the model. The uncertainty in retrieved updraft velocities was estimated through point-for-point comparison of the scaled retrievals with model updrafts. For updraft velocities larger than 1 $\mathrm{m\ s^{-1}}$ (as analysed in this study), a root-mean-square difference of 2.5 $\mathrm{m\ s^{-1}}$ was found. It is likely that this uncertainty introduces scatter into the relationships between ε and characteristics of updraft velocity presented in Section 6, resulting in weaker measured correlations than may exist between ε and the true updraft strength.

2.2 Dissipation rates from CAMRa

Doppler weather radar, such as CAMRa, can be used to infer characteristics of atmospheric turbulence from observations of the radial velocity field. The mean Doppler velocity $\bar{v}$, is the

reflectivity-weighted average of radial point velocities found within a resolution volume (the volume of atmosphere observed by a single radar pulse, V_6). The Doppler spectrum variance σ_v^2, estimated by CAMRa, is the variance in the velocity of reflectors within V_6. Therefore, σ_v^2 includes velocity variance due to the turbulent motion of hydrometeors, among contributions from several other mechanisms. We assume that σ_v^2 can be decomposed into a sum of statistically independent variance contributions (Doviak and Zrnic, 1984).

$$\sigma_v^2 = \sigma_s^2 + \sigma_\mathrm{t}^2 + \sigma_\mathrm{TV}^2 + \sigma_\alpha^2 + \sigma_\mathrm{o}^2 \tag{1}$$

Where σ_v^2 has contributions primarily from radial wind shear across the sample volume σ_s^2, turbulence σ_t^2, the distribution of hydrometeor fall-velocities σ_TV^2, antenna rotation σ_α^2, and hydrometeor oscillations σ_o^2.

Using the theoretical framework presented by Frisch and Clifford (1974), we can calculate the eddy dissipation rate, ε from σ_t^2. Details of turbulent motion cannot be directly measured from σ_v^2. We can only infer σ_t^2 from σ_v^2 by accounting for all other variance contributions in (1), either by subtracting their variance from σ_v^2, or by demonstrating that they are negligibly small compared to σ_t^2.

The eddy dissipation rate is the rate of energy transfer through the inertial sub-range of isotropic turbulence. For calculations of ε to be accurate, σ_t^2 must consist only of velocity variance due to eddies with a spatial scale less than the largest scale of the inertial sub-range, Λ_0. Ensuring this involves the careful separation of shear and turbulence, which is summarised in Section 5.

Once σ_t^2 has been determined, ε can be estimated from,

$$\varepsilon \approx \frac{1}{\alpha}\left[\frac{\sigma_\mathrm{t}^2}{1.35A\left(1-\frac{\gamma^2}{15}\right)}\right]^{\frac{3}{2}} \tag{2a}$$

$$\varepsilon \approx \frac{1}{\beta}\left[\frac{\sigma_t^2}{1.35A\left(1+\frac{\xi^2}{15}\right)}\right]^{\frac{3}{2}} \quad (2b)$$

Where α (in metres) is the angular standard deviation of the two-way Gaussian beam pattern in the transverse (or elevation) direction (see σ_2 in Appendix S1), multiplied by the range from the radar. β is the standard deviation of the pulse in the radial dimension (assumed uniform; for CAMRa $\beta =$ 26.25m). From this, $\gamma^2 = 1 - \left(\frac{\beta}{\alpha}\right)^2$ and $\xi^2 = 1 - \left(\frac{\alpha}{\beta}\right)^2$, and A is the universal constant of inertial sub-range turbulence, with a value of 1.6.

If $\alpha > \beta$, then (2a) is used, with (2b) to be used if $\alpha < \beta$. This distinction has often been ignored in past studies, which typically employ a simplified version of (2a) to determine ε (as stated in Doviak and Zrnic (1984)). For CAMRa, $\alpha > \beta$ at all ranges further than 17.9 km from the radar, so a similar approximation could be used. However, the application of (2a) and (2b) is straight-forward and any further approximation should be unnecessary.

Values of σ_v^2 generally range from 1 – 25 $m^2\ s^{-2}$ in our observations. In reality, the negligibility of terms in (1) depends on their value relative to σ_t^2, and as a result, no fixed variance value will always be negligibly small. Assuming that turbulence is only significant when $\sigma_t^2 > 5\ m^2\ s^{-2}$ (this translates to $\varepsilon > 0.03\ m^2\ s^{-3}$ when $\alpha = \beta$), we choose a negligibility threshold σ_{neg}^2, of 0.5 $m^2\ s^{-2}$ for the purpose of this application. Whereby, variance contributions that are less than σ_{neg}^2 can be neglected. We can test the impact of this selection on ε by determining the maximum combined variance of terms we may neglect. The variance contribution from σ_α^2 is small enough to be ignored completely ($\sigma_\alpha^2 < 0.01\ m^2\ s^{-2}$, see Section 4). We can calculate σ_s^2 directly (Section 5), so no element of this contribution is neglected, regardless of value compared to σ_{neg}^2. However, contributions from σ_{TV}^2 and σ_o^2 are not simple to measure directly in our observations. Contributions from σ_{TV}^2 can be larger than σ_{neg}^2 for rain and hail (Section 3), while σ_o^2 is generally less than 0.25 $m^2\ s^{-2}$ (Section 4). A maximum error would be incurred in σ_t^2 of 0.75 $m^2\ s^{-2}$ when neglecting

206 σ_{TV}^2 at 0.5 $\mathrm{m^2\ s^{-2}}$ (in the extreme case that hail or heavy rain is observed very close to the radar) and
207 σ_{o}^2 at 0.25 $\mathrm{m^2\ s^{-2}}$. If $\sigma_{\mathrm{t}}^2 = 5\ \mathrm{m^2\ s^{-2}}$, this would translate to a 21.6% positive error in ε. The error
208 decreases as turbulence becomes more significant, to only 4.5% when $\sigma_{\mathrm{t}}^2 = 25\ \mathrm{m^2\ s^{-2}}$, and is
209 independent of the range of the σ_{t}^2 observation.

210 The range of ε values we can estimate using the Doppler spectrum width technique is determined
211 from the range of σ_v^2 values we can observe. This is related to the maximum ambiguous velocity
212 interval (Nyquist velocity) of the radar. Keeler and Passarelli (1990) state that reliable measurements
213 of the Doppler spectrum width can only be made between 0.02 – 0.2 of the Nyquist interval. CAMRa
214 has a Nyquist interval of 30 $\mathrm{m\ s^{-1}}$, so we can only reliably observe σ_v between 0.6 – 6 $\mathrm{m\ s^{-1}}$,
215 corresponding to σ_v^2 of 0.36 – 36 $\mathrm{m^2\ s^{-2}}$. In the case where $\sigma_t^2 = \sigma_v^2$, we can determine the maximum
216 detectable range in ε from using this method with CAMRa. If observing such a range in σ_t^2 at a range
217 of 50 km, (the typical range of our storm observations), this would correspond to a maximum
218 detectable range in ε of $10^{-3} - 1\ \mathrm{m^2\ s^{-2}}$.

219 The following three sections outline methods to assess the contribution of the non-turbulent terms
220 in (1). By either calculating these terms directly, or showing that they are negligibly small compared
221 to σ_{t}^2, we can remove them from σ_v^2. This allows us to find σ_{t}^2 as a residual velocity variance, and
222 then convert this to ε using (2a) and (2b).

223

224 ## 3 Doppler variance due to a distribution of hydrometeor fall velocities, σ_{TV}^2

225 ### *3.1 Theoretical framework and derivation of spectral variance equations*

226 In a given sample volume V_6, the presence of a distribution of hydrometeor diameters will lead to
227 a distribution of hydrometeor fall velocities. In the circumstance where the radar beam is not
228 perpendicular to hydrometeor velocity, this broadens the Doppler velocity spectrum. The observed
229 variance contribution, σ_{TV}^2 in (1), is at its maximum for a vertically pointing radar beam and decreases

with angle from zenith. Values of σ_v^2 include the total variance of hydrometeor velocity within the pulse volume. According to (1), the variance in hydrometeor velocity from a fall-speed distribution (σ_{TV}^2) is statistically independent from the variance in hydrometeor velocity resulting from air motions within the cloud (included in σ_s^2 and σ_{t}^2). Consequently, we require no assumptions regarding the vertical motion of air within the cloud when estimating σ_{TV}^2.

Previous studies to estimate turbulence characteristics from Doppler velocity spectra typically assume σ_{TV}^2 to be negligible (e.g. Frisch and Clifford, 1974; Chapman and Browning, 2001; Meischner *et al*., 2001; Melnikov and Doviak (2009)) unless observations were made at vertical incidence (Brewster and Zrnic, 1986). The expected variance due to σ_{TV}^2 is reduced significantly by scanning at lower elevations (often the reason σ_{TV}^2 is assumed negligible), however, this does not ensure the contribution is always negligibly small. Melnikov and Doviak (2009) neglected variance contributions from σ_{TV}^2 purely by assuming they remained below 0.2 $\mathrm{m^2\ s^{-2}}$ when scanning at elevations below 20° through stratiform precipitation. However, results presented in Section 3.2 suggest σ_{TV}^2 from raindrops can reach 1 $\mathrm{m^2\ s^{-2}}$ when scanning at 20°, though this remains dependent on radar reflectivity. The objectives of this section are to: provide a means to estimate σ_{TV}^2 when required, provide justification when neglecting σ_{TV}^2 contributions (showing that $\sigma_{\mathrm{TV}}^2 < \sigma_{\mathrm{neg}}^2$), and inform how future scanning strategies for turbulence retrieval can be tailored to ensure σ_{TV}^2 is always negligible.

For application to RHI radar observations, we classify two hydrometeor types based on the height of the 0°C isotherm, $z_{0°\mathrm{C}}$, which is estimated from the location of bright-band radar reflectivity in our observations. Though $z_{0°\mathrm{C}}$ varies for different DYMECS case days, the average height is ~ 1.5 km. For simplicity, we assume any reflectivity returned from below this level is due to liquid raindrops, and any reflectivity from above is due to ice aggregates. By making this simple distinction, we can estimate σ_{TV}^2 in all areas of an RHI scanning domain. In addition to aggregates and raindrops, graupel and hail are also important hydrometeor types, especially in convective clouds. We therefore

extend our analysis to assess the impact of hail, and consider the effects of graupel (treated as low-density hailstones) in Section 3.3.

We assume the reflectivity for a given V_6 is dominated by one hydrometeor type, and that hydrometeors are falling vertically downwards at terminal velocity relative to the vertical air motions within the cloud. We assume hailstones are dry and are of solid ice with homogeneous density. For hydrometeor mass calculations, we assume that both raindrops and hailstones are spherical.

To estimate the relative size of σ^2_{TV} when compared to σ^2_v, we can characterise σ^2_{TV} as the variance of the reflectivity-weighted mean fall velocity in V_6 as,

$$\sigma^2_{\mathrm{TV}_j} = \overline{W_j^2} - \bar{W}_j^2, \tag{3}$$

where $\sigma^2_{TV_j}$ has units $\mathrm{m^2 s^{-2}}$, W is the reflectivity-weighted hydrometeor fall velocity, and j refers to the hydrometeor type. We estimate $\overline{W_j^2}$ and $\bar{W}_j^2$ by evaluating the following integrals,

$$\overline{W_j^2} = \frac{\int_0^\infty V_j(D)^2\, M_j(D)^2\, n_j(D)\, dD}{\int_0^\infty M_j(D)^2\, n_j(D)\, dD}, \tag{4}$$

$$\bar{W}_j^2 = \left(\frac{\int_0^\infty V_j(D)\, M_j(D)^2\, n_j(D)\, dD}{\int_0^\infty M_j(D)^2\, n_j(D)\, dD} \right)^2, \tag{5}$$

where $V_j(D)$, $M_j(D)$ and $n_j(D)$ are terminal velocity-diameter, mass-diameter and particle-size distribution (DSD) relationships for hydrometeor j, respectively, and D is the hydrometeor diameter in metres.

In (4) and (5), we assume that particle reflectivity is proportional to $M_j(D)^2$. We are in the Rayleigh scattering regime, and hence this is a reasonable assumption for a 3 GHz radar. The integral $R_j \int_0^\infty M_j(D)^2\, n_j(D)\, dD$ provides the radar reflectivity in $\mathrm{mm^6\ m^{-3}}$. The term R_j is cancelled out in (4) and (5), but is given by,

$$R_j = 10^{18} \frac{\left|K_j\right|^2}{|K_{\text{water}}|^2} \left(\frac{6}{\pi \rho_j}\right)^2 , \quad (6)$$

where $\left|K_j\right|^2$ and ρ_j are the dielectric factor and density of hydrometeor j.

Terminal velocity-diameter relationships are commonly expressed as simple power laws,

$$V_j(D) = p_j D^{q_j} , \quad (7)$$

where V is the fall velocity and D is the drop diameter. For ice aggregates, D is the melted diameter. Values of p and q for raindrops, ice aggregates and hailstones are taken from Atlas and Ulbricht (1977), Gunn and Marshall (1958) and Cheng and English (1982), respectively. These have been converted into S. I. units (See Table 1).

The hydrometeor mass M, as a function of particle diameter D, can be expressed in the form,

$$M_j(D) = a_j D^{b_j} \quad (8)$$

where M and D are in S. I. units.

We assume that the DSD of each hydrometeor class can be approximated by an exponential distribution of form given by Marshall and Palmer (1948).

$$n_j(D) = N_{0_j} \exp\left(-\lambda_j D\right) \quad (9)$$

Where N_{0_j} and λ_j are the intercept ($n_j(D = 0)$) and slope parameters, respectively, for hydrometeor type j. We consider this a suitable approximation; spectral broadening owing to a distribution in fall velocity has been shown to be nearly independent of the precise shape of the size distribution (Lhermitte, 1963).

For rain and ice aggregates, values of ρ, $|K|^2$, a, b and N_0, are sourced from the UK Met Office

Unified Model microphysics scheme, as summarised in Stein *et al*. (2014) (See Table 1). For hail, we use an N_0 of 1.2 $\times$ 10^4 m^{-4} taken from Waldvogel *et al*. (1978). The sensitivity of $\sigma^2_{\mathrm{TV}_j}$ to N_{0_j} is discussed in Section 3.3.

To evaluate (3), we first substitute (7) – (9) into (4) and (5) using values from Table 1. By using a gamma function solution for the integrals in (3) we derive expressions for Doppler spectral variance contribution for the three hydrometeor varieties. At this point, they are functions only of DSD parameter, λ_j. Stein *et al*. (2014) provide an expression relating λ_j to radar reflectivity, Z_j,

$$\lambda_j = \left(\frac{R_j a_j^2 N_{0_j} \Gamma\left(1 + 2b_j\right)}{Z_j} \right)^{\frac{1}{1+2b_j}}, \tag{10}$$

where Z_j is the radar reflectivity of hydrometeor j and has linear units of $\mathrm{mm}^6\ \mathrm{m}^{-3}$.

Substituting (10) into the $\sigma^2_{\mathrm{TV}_j}(\lambda_j)$ expressions and simplifying using values from Table 1, produces spectral variance equations for rain, ice aggregates and hail,

$$\sigma^2_{\mathrm{TV}_{\mathrm{rain}}} = 0.62\, Z^{0.191} \sin^2 \theta_{\mathrm{el}}\ , \tag{11}$$

$$\sigma^2_{\mathrm{TV}_{\mathrm{agg}}} = 0.029\, Z^{0.119} \sin^2 \theta_{\mathrm{el}}\ , \tag{12}$$

$$\sigma^2_{\mathrm{TV}_{\mathrm{hail}}} = 1.7\, Z^{0.143} \sin^2 \theta_{\mathrm{el}}\ , \tag{13}$$

Where Z is in $\mathrm{mm}^6\ \mathrm{m}^{-3}$, $\sigma^2_{\mathrm{TV}_j}$ has units of $\mathrm{m}^2\ \mathrm{s}^{-2}$ and θ_{el} is the elevation angle of the reflectivity observation measured from the surface. Together, these expressions can be used to estimate the Doppler variance contribution due to the distribution of hydrometeor fall speeds in V_6.

3.2 Analysis of $\sigma^2_{\mathrm{TV}_j}$

Reflectivity measurements in our observations with CAMRa are generally no less than -20 dBZ (the minimum detectable echo at 10 km range), and no more than 60 dBZ. In our application, we

315 therefore classify $\sigma^2_{\mathrm{TV}_j}(Z_j = -20\ \mathrm{dBZ})$ and $\sigma^2_{\mathrm{TV}_j}(Z_j = 60\ \mathrm{dBZ})$ as the minimum and maximum
316 potential variances we encounter from each hydrometeor type.

317 Equations (11) – (13) show that $\sigma^2_{\mathrm{TV}_j}$ increases with radar reflectivity and elevation angle of
318 observation. Assuming a vertically pointing radar beam, and given Z_j in the range of -20 dBZ to 60
319 dBZ, $\sigma^2_{\mathrm{TV}_{\mathrm{rain}}}$ increases from 0.26 to 8.62 $\mathrm{m^2\ s^{-2}}$, $\sigma^2_{\mathrm{TV}_{\mathrm{agg}}}$ from 0.02 to 0.15 $\mathrm{m^2\ s^{-2}}$ and $\sigma^2_{\mathrm{TV}_{\mathrm{hail}}}$ from
320 0.90 to 12.53 $\mathrm{m^2\ s^{-2}}$. For DYMECS observations, RHIs scanned at a maximum elevation angle of
321 15°. Figure 1a displays (11) – (13) for a vertically pointing beam (black lines) and for 15° elevation
322 (grey lines). Compared with a vertically pointing beam, if Z_j is sampled at 15° elevation, values of
323 $\sigma^2_{\mathrm{TV}_j}$ are respectively reduced by a factor of 14.

324 A maximum $\sigma^2_{\mathrm{TV}_{\mathrm{agg}}}$ of 0.15 $\mathrm{m^2\ s^{-2}}$ suggests that the contribution from ice aggregates is always
325 less than σ^2_{neg}. Assuming that ice aggregates constitute all hydrometeors above $z_{0°\mathrm{C}}$, then σ^2_{TV} is
326 negligible for all observations made above this level. For rain observations, which we assume are
327 limited to below $z_{0°\mathrm{C}}$, the equivalent maximum of 8.62 $\mathrm{m^2\ s^{-2}}$ is comparably large, and so $\sigma^2_{\mathrm{TV}_{\mathrm{rain}}}$
328 cannot always be neglected. Using (11), we see $\sigma^2_{\mathrm{TV}_{\mathrm{rain}}}(60\ \mathrm{dBZ}) < \sigma^2_{\mathrm{neg}}$ for all rain observed at $\theta_{\mathrm{el}} <$
329 13.9°.

330 Under the circumstances that: $\sigma^2_{\mathrm{TV}_{\mathrm{agg}}}$ is always negligible, $\sigma^2_{\mathrm{TV}_{\mathrm{rain}}}$ is negligible when $\theta_{\mathrm{el}} < 13.9°$,
331 $z_{0°\mathrm{C}}$ can be estimated, and hail is not present, we can describe the negligibility of σ^2_{TV} in terms of a
332 minimum range from the radar, R_{min}. For our application, R_{min} is simply the range from the radar a
333 pulse reaches a height of $z_{0°\mathrm{C}}$ when transmitted at $\theta_{\mathrm{el}} < 13.9°$. In our RHI observations (where
334 $z_{0°\mathrm{C}} \sim 1.5$ km), σ^2_{TV} is negligibly small everywhere at ranges further than 6.1 km from the radar.
335 While σ^2_{TV} can still be significant due to rain occurring nearer than R_{min}, below $z_{0°\mathrm{C}}$, it remains
336 conditional on both Z_{rain} and θ_{el}. Observations used in this application were rarely made closer than
337 30 km from the radar, and so we neglect σ^2_{TV} for rain and ice aggregates.

According to (13), hail can contribute more to σ_v^2 than rain. However, hail is generally a much less common, more localised occurrence than rain. As a result, the detection of hail using retrieved radar parameters (e.g. hail differential reflectivity H_{DR}, Depue *et al*. (2007)) is necessary before (13) can be reliably applied. If observations do indeed include hail, (13) suggests that $\sigma^2_{\mathrm{TV}_{\mathrm{hail}}}(60\ \mathrm{dBZ})$ falls below σ^2_{neg} for all hail observations made at $\theta_{\mathrm{el}} < 11.5°$. Due to the potential for hail presence both above and below $z_{0°\mathrm{C}}$, negligibility based on range from radar is not stated. However, as the minimum range of observations was 30 km, hail would need to be observed at 6 km altitude for $\sigma^2_{\mathrm{TV}_{\mathrm{hail}}}$ to exceed σ^2_{neg}, which is unlikely to have occurred.

Based on our threshold for negligibility σ^2_{neg}, the estimation of $z_{0°\mathrm{C}}$, and under the assumptions made in the derivation of (11) – (13), we can neglect variance contributions from σ^2_{TV} in our observations. Due to the dependence of (11) – (13) only on Z and θ_{el}, we expect this conclusion to hold true for other scanning weather radars.

3.3 Sensitivity of $\sigma^2_{\mathrm{TV}_{\mathrm{rain}}}$ and $\sigma^2_{\mathrm{TV}_{\mathrm{hail}}}$ to assumptions

In this section, we examine the sensitivity of our results to some of the assumptions made in the derivation of (11) and (13). For ice aggregates, no reasonable sensitivity testing has resulted in the factor 3 increase in $\sigma^2_{\mathrm{TV}_{\mathrm{agg}}}$ required to even conditionally exceed σ^2_{neg}. As a result, sensitivity tests involving ice aggregates have been omitted from this discussion, and we conclude that $\sigma^2_{\mathrm{TV}_{\mathrm{agg}}}$ is always negligible.

For rain and hail, we expect little uncertainty in the majority of values in Table 1. The first potential source of uncertainty lies with the treatment of hail as dry with the density of solid ice. We compare $\sigma^2_{\mathrm{TV}_{\mathrm{hail}}}$ when hailstones are dry with the density of solid ice (assumed in (13)), to low-density and melting hailstones. Melting hailstones will possess a thin outer layer of liquid water, appearing to the radar as large raindrops. To simulate this effect, we change the dielectric factor

362 $|K_{\mathrm{hail}}|^2$, in (6) from 0.174 to 0.93. Resulting variance contributions are 21% lower than for dry
363 hailstones for any given reflectivity. Assuming all hailstones below $z_{0°\mathrm{C}}$ have a liquid water layer,
364 this reduction leads to $\sigma^2_{\mathrm{TV}_{\mathrm{hail}}}(60\ \mathrm{dBZ}) \approx \sigma^2_{\mathrm{TV}_{\mathrm{rain}}}(60\ \mathrm{dBZ})$ below $z_{0°\mathrm{C}}$. For observations made below
365 $z_{0°\mathrm{C}} = 1.5$ km, we find that $\sigma^2_{\mathrm{TV}} < \sigma^2_{\mathrm{neg}}$ at all ranges further than 6.5 km from the radar, regardless
366 of hydrometeor type. If we further consider melting hailstones consisting of low-density ice that is
367 more consistent with graupel ($\rho_{\mathrm{hail}} = 500\ \mathrm{kg\ m^{-3}}$), this leads to a combined reduction in $\sigma^2_{\mathrm{TV}_{\mathrm{hail}}}$ of
368 34%, at which point $\sigma^2_{\mathrm{TV}_{\mathrm{hail}}}(60\ \mathrm{dBZ}) < \sigma^2_{\mathrm{TV}_{\mathrm{rain}}}(60\ \mathrm{dBZ})$, and we revert to neglecting σ^2_{TV} at ranges
369 further than 6.1 km.

370 A second source of uncertainty lies with the chosen values of N_0; respective values for rain and
371 hail are assumed constant. For rain, we use $N_{0_{\mathrm{rain}}} = 8 \times 10^6\ \mathrm{m^{-4}}$ from Marshall and Palmer
372 (1948), who demonstrate its independence of rainfall intensity. The assumption of a constant $N_{0_{\mathrm{hail}}}$
373 is not as safe as for raindrops as it depends on the largest hail diameter, D_{max}, and has been shown
374 to vary from 10^3 – $10^5\ \mathrm{m^{-4}}$ (Ulbricht, 1974). Our chosen value of $N_{0_{\mathrm{hail}}} = 1.2 \times 10^4\ \mathrm{m^{-4}}$ from
375 Waldvogel *et al*. (1978) is roughly in the centre of this range, and is very similar to values of $1.1 -$
376 $1.4 \times 10^4\ \mathrm{m^{-4}}$ presented by Ulbricht (1977). We test the effect of decreasing values of N_0 for rain
377 and hail by an order of magnitude. This decrease is chosen to be large enough to roughly account for
378 the maximum potential variability in N_0. The result is a 55% increase in $\sigma^2_{\mathrm{TV}_{\mathrm{rain}}}$ and a 39% increase
379 in $\sigma^2_{\mathrm{TV}_{\mathrm{hail}}}$. Such a large increase in $\sigma^2_{\mathrm{TV}_{\mathrm{rain}}}$ is unlikely given the confidence in our selection of $N_{0_{\mathrm{rain}}}$
380 (Marshall and Palmer, 1948). However, the corresponding increase for $\sigma^2_{\mathrm{TV}_{\mathrm{hail}}}$ is more likely realised
381 given the stated uncertainty in $N_{0_{\mathrm{hail}}}$. Such an increase would imply that $\sigma^2_{\mathrm{TV}_{\mathrm{hail}}}(60\ \mathrm{dBZ}) < \sigma^2_{\mathrm{neg}}$
382 only if observed at $\theta_{\mathrm{el}} < 9.8°$. By instead increasing values of N_0 by an order of magnitude (not
383 shown), we see a reduction in $\sigma^2_{\mathrm{TV}_{\mathrm{hail}}}$ and $\sigma^2_{\mathrm{TV}_{\mathrm{rain}}}$ of 36% and 28%, respectively.

384 A final source of uncertainty lies with the selected velocity-diameter relationship for hail,
385 $V_{\mathrm{hail}}(D)$. There is a broader diversity in these relationships in the literature than for rain; we assume

386 the $\mathrm{V_{rain}(D)}$ power law provided by Atlas and Ulbricht (1977) to be accurate. Figure 1b compares
387 $\sigma^2_{\mathrm{TV_{hail}}}$ from (13) derived using $V_{\mathrm{hail}}(D)$ from Cheng and English (1982), Ulbricht (1977), and
388 Pruppacher and Klett (1978). As the $V_{\mathrm{hail}}(D)$ proposed by Ulbricht (1977) involves the same
389 exponent ($q = 0.5$) as that used for (13), the resulting effect is a 29% increase in $\sigma^2_{TV_{\mathrm{hail}}}$ for all
390 reflectivity owing to the different values of p. The $V_{\mathrm{hail}}(D)$ relationship from Pruppacher and Klett
391 (1978) however, involves $q = 0.8$. This leads to a change in exponent in (13), causing a decrease in
392 $\sigma^2_{\mathrm{TV_{hail}}}(Z < 40\ \mathrm{dBZ})$ and an increase for $\sigma^2_{\mathrm{TV_{hail}}}(Z > 40\ \mathrm{dBZ})$. $\sigma^2_{\mathrm{TV_{hail}}}(60\ \mathrm{dBZ})$ is increased by 43%.
393 Figure 1b suggests that the selection of $V_{\mathrm{hail}}(D)$ can have a substantial and varied effect on $\sigma^2_{\mathrm{TV_{hail}}}$
394 which somewhat limits how precisely we can state the conditions that allow us to neglect $\sigma^2_{\mathrm{TV_{hail}}}$.
395

396 **4 Spectral variance due to antenna rotation, σ^2_α and hydrometeor oscillations, σ^2_{o}.**

397 The movements of the radar antenna while scanning will broaden the Doppler spectrum.
398 Assuming a constant antenna scan rate α, in $\mathrm{rad\ s^{-1}}$, the spectral variance contribution due to antenna
399 rotation is provided by Doviak and Zrnic (1984),

400 $$\sigma^2_\alpha = \left(\frac{\alpha\lambda \cos\theta_{\mathrm{el}} \sqrt{\ln(2)}}{2\pi\theta_1}\right)^2 , \qquad (14)$$

401 where λ is the wavelength of the radar in metres, θ_{el} is the elevation angle from the surface, and θ_1
402 is the one-way half-power beam width in radians.

403 For CAMRa, $\lambda = 0.0975\ \mathrm{m}$ and $\theta_1 = 5 \times 10^{-3}\ \mathrm{rad}$. During DYMECS, RHI and PPI
404 observations were made using scan speeds of $\alpha_{\mathrm{RHI}} = 7 \times 10^{-3}\ \mathrm{rad\ s^{-1}}$ and $\alpha_{\mathrm{PPI}} = 35 \times$
405 $10^{-3}\ \mathrm{rad\ s^{-1}}$. The contribution from σ^2_α is largest when scanning horizontally ($\cos(\theta_{\mathrm{el}} = 0) = 1$);
406 in this case $\sigma^2_\alpha < 0.01\ \mathrm{m^2\ s^{-2}}$ for both RHI and PPI observations, making a negligible ($\sigma^2_\alpha < \sigma^2_{\mathrm{neg}}$)
407 contribution to σ^2_v. Observations collected at non-zero elevations (up to 15° in DYMECS) would

only reduce the value of σ_α^2. Equation (14) can be used simply to determine the contribution of σ_α^2 for radars with much faster scanning speeds.

The oscillation of hydrometeors can contribute to σ_v^2, and has been speculated in Zrnic and Doviak (1989) to lead to over-estimation of ε. They find that σ_o^2 decreases with rain-rate, and generally does not increase above 0.25 $\mathrm{m^2\ s^{-2}}$, so we neglect these contributions.

5 Spectral broadening due to shear of the radial wind, σ_s^2

5.1 Spectral variance equations for shear

Since we are justified in neglecting σ_TV^2, σ_α^2 and σ_o^2 in (1) for DYMECS observations, we are left with Doppler variance contributions from shear and turbulence. We can derive the turbulent contribution from,

$$\sigma_\mathrm{t}^2 = \sigma_v^2 - \sigma_s^2 \,, \tag{15}$$

for use in (2a) and (2b) to calculate ε.

In (15), σ_s^2 represents the sum of Doppler variance contributions from the shear of the radial wind in the elevation θ, azimuthal (transverse across the beam) φ, and radial r, directions. Similar to σ_v^2, σ_s^2 can be decomposed into a sum of statistically independent variance contributions from shear in each direction.

$$\sigma_s^2 = \sigma_{s\theta}^2 + \sigma_{s\varphi}^2 + \sigma_{sr}^2 \tag{16}$$

Various equations have been used in past literature to calculate $\sigma_{s\theta}^2$ and $\sigma_{s\varphi}^2$ that are not mutually consistent (e.g. Chapman and Browning, 2001). In Appendix S1, we provide a derivation of these equations that produces results in agreement with those stated in Doviak and Zrnic (1984). An expression for σ_{sr}^2 is also taken from Doviak and Zrnic (1984), assuming a rectangular transmitted pulse.

$$\sigma_{s\theta}^2 = \frac{(|S_\theta| R\theta_1)^2}{16 \ln 2} \quad (17)$$

$$\sigma_{s\varphi}^2 = \frac{\left(|S_\varphi| R\theta_1\right)^2}{16 \ln 2} \quad (18)$$

$$\sigma_{sr}^2 = \left(\frac{0.35|S_r| c\tau}{2}\right)^2 \quad (19)$$

Where R is the radial distance from the radar in metres, c is the speed of light in m s^{-1}, and τ is the pulse duration in seconds (for CAMRa, $\tau = 0.5$ μs). $|S_\theta|$, $|S_\varphi|$ and $|S_r|$ are shear magnitudes in s^{-1}, calculated from the mean Doppler velocity field. In (17) – (19), velocity and reflectivity gradients are assumed to be linear across V_6. Equations (17) and (18) differ only in the shear involved, as the beam profiles in the θ and φ dimensions are the same.

In application to CAMRa, the variability of $\sigma_{s(\theta,\varphi,r)}^2$ with $|S|$ and R is illustrated in Figure 1c. For $|S_r|$ in the range of 0 to 0.02 s^{-1}, σ_{sr}^2 increases with $|S_r|^2$ from 0 to 0.28 m^2 s^{-2}. As the pulse length is constant, σ_{sr}^2 does not vary with range. If $|S_r| < 0.027$ s^{-1} then $\sigma_{sr}^2 < \sigma_{\text{neg}}^2$, indicating that for our observations, σ_{sr}^2 is negligibly small except in cases of extreme shear. However, although σ_{sr}^2 is likely to be small, our chosen method of calculating shear (Section 5.3) permits direct measurement of $|S_r|$ to be made simply. We therefore include contributions from σ_{sr}^2 in σ_s^2.

At 30 km range, for $|S_{\theta,\varphi}|$ in the range of 0 – 0.02 s^{-1}, $\sigma_{s(\theta,\varphi)}^2$ increases from 0 – 0.75 m^2 s^{-2}. At 150 km range, this increase is to 18.7 m^2 s^{-2} when $|S_{\theta,\varphi}|$ is 0.02 s^{-1}. This suggests that, even at the minimum range of 30 km, if $|S_{\theta,\varphi}| > 0.016$ s^{-1}, then $\sigma_{s(\theta,\varphi)}^2$ is always greater than σ_{neg}^2 for our data. Given that shears of this magnitude are quite possible (especially in the elevation direction), $\sigma_{s(\theta,\varphi)}^2$ will need to be considered for all of our observations. The high resolution of CAMRa means that radial velocity shear measured over small distances often result in negligible (less than 0.5 m^2 s^{-2}) contributions to σ_v^2, however, as illustrated, this is not true for shear of sufficient values. To ensure

accuracy in point-to-point values of ε, and consistency in application across full RHI scans, we measure and remove σ_s^2 at each point in our data. In Section 6.2, we provide and discuss an example retrieval for a shower cloud (Figure 8) in which σ_s^2 exceeds σ_{neg}^2 quite widely and represents a significant proportion of σ_{t}^2. This example is used to highlight the potential for significant over-estimation of ε in our cases if shear corrections are neglected.

5.2 Separation of shear and turbulence - theory

The separation of shear and turbulence is a significant challenge. However, methods to make this distinction are guided by the framework employed to derive ε from σ_v^2 summarised in Section 2.2. The calculation of σ_s^2 is necessary to remove velocity variance contributions to σ_v^2 from outside the range of scales sampled by the radar. The scale over which to calculate shear (hereafter referred to as Λ_s) in (17) – (19), should ideally be equal to the largest scale of the inertial sub-range, Λ_0. However, Λ_s should be strictly no larger than Λ_0, otherwise the inclusion in σ_{t}^2 of variance from outside the inertial sub-range will lead to an over-estimation of ε.

Without the means to routinely estimate Λ_0 for each of the convective storm observations collected in DYMECS, we refer to past literature. Past studies have utilised Doppler spatial spectra and aircraft measurements to estimate Λ_0 in individual convective clouds (Battan, 1975; Knupp and Cotton, 1982; Brewster and Zrnic, 1986). They found that Λ_0 can be as large as 1.5 – 3 km. These estimates were made in severe thunderstorms/hailstorms with strong, large-scale circulations. In comparison, the convective storms constituting the DYMECS observations are generally much weaker, limiting how applicable these values are to our cases. We assume Λ_0 scales with the size of the largest eddy-generating mechanisms in a convective cloud, i.e. the main updraft circulation. If this circulation is shallow, we expect Λ_0 to be small as the downscale cascade to isotropic turbulence begins at a smaller eddy scale. As updraft heights on DYMECS case days generally ranged from 3 – 8 km (Nicol *et al*., 2015), we assume $\Lambda_0 \sim 1$ km for this application. Chapman and Browning (2001) found a factor two change in Λ_0 to have very little effect on their resulting values of ε. However, this

involved assuming a Λ_0 of only 200 m for shallow shear layers, so we test the sensitivity of our retrieved ε to the value of Λ_s, summarised in Section 5.5.

5.3 Separation of shear and turbulence – linear velocity surface approach

The application of methods to distinguish σ_s^2 from σ_t^2 will depend on the relationship between the spatial resolution of the radar and Λ_0. As long as the largest dimension of V_6 is less than Λ_0, σ_t^2 can be used to estimate ε (Frisch and Clifford, 1974). As this is generally the case for a radar of CAMRa's resolution, scanning deep convective clouds, σ_s^2 can then be determined from radial velocity shear calculated over enough contiguous V_6 volumes to constitute a spatial scale of Λ_0.

To evaluate shear over a constant spatial scale in data with polar co-ordinates is not straightforward. With two-dimensional radar data, the most effective way to achieve this is to use least-squares regression to fit a velocity surface to Doppler velocity data. A suitable framework for this velocity surface is taken from Neter and Wasserman (1974), and has been applied in previous ε-retrieval studies (Istok and Doviak 1986, Meischner *et al*., 2001). When applied to RHIs, the velocity surface is given by

$$V_i = V_0 + S_\theta \, l_{\theta_i} + S_r l_{r_i} + E_i \tag{20}$$

where

$$l_{\theta_i} = R_0(\theta_i - \theta_0) \quad ; \quad l_{r_i} = R_i - R_0$$

The range from the radar is given by R, θ is the elevation angle in radians, and (θ_0, R_0) is the centre point of the surface. V_i is the radial velocity at the point (θ_i, R_i), and E_i is the velocity difference between the data and the surface. V_0 is the estimated central point velocity and S_θ and S_r are linear elevation and radial shears, respectively. l_{θ_i} and l_{r_i} are the elevation and radial distances between V_i and V_0.

500 The parameters V_0, S_θ and S_r are determined from the matrix operation,

501
$$\begin{bmatrix} V_0 \\ S_\theta \\ S_r \end{bmatrix} = \begin{bmatrix} n & \sum l_{\theta_i} & \sum l_{r_i} \\ \sum l_{\theta_i} & \sum l_{\theta_i}^2 & \sum l_{r_i} l_{\theta_i} \\ \sum l_{r_i} & \sum l_{\theta_i} l_{r_i} & \sum l_{r_i}^2 \end{bmatrix}^{-1} \begin{bmatrix} \sum V_i \\ \sum V_i l_{\theta_i} \\ \sum V_i l_{r_i} \end{bmatrix} \quad (21)$$

502 Centred to best approximation on a chosen Doppler velocity point, neighbouring data points are
503 used to constitute (as closely as is possible) a Λ_s – by – Λ_s grid of data, G. Using velocities from G,
504 (21) is used to compute linear shears S_θ and S_r, which are attributed back to the data point at the
505 centre of G. By completing this process for all points in a scan, we obtain fields of S_θ and S_r,
506 calculated over a fixed scale. If $\Lambda_s = \Lambda_0$, S_θ and S_r are representative of large eddies and/or velocity
507 gradients in the ordered background flow. As a result, they can be used in (17) and (19) to determine
508 $\sigma_{s\theta}^2$ and σ_{sr}^2.

509 In applying (20) to our observations, we find that data located less than ~ $\frac{\Lambda_s}{2}$ from the edge of
510 observed clouds will be lost in surface fitting. The grid G will only be partially filled with data for
511 those V located on the periphery of reflectivity echoes, meaning (21) cannot be performed. The
512 degree of data loss therefore increases with the value of Λ_s. As we can only account for σ_s^2 where
513 shear can be measured, this data loss is imposed on retrieved fields of ε. Consequently, this limits
514 our ability to investigate values of ε associated with entrainment processes near cloud edges.
515 However, turbulence associated with entrainment into updrafts can still be retrieved in cases where
516 updrafts are further than ~ $\frac{\Lambda_s}{2}$ from the edge of the radar echo (e.g. Figure 6c and 6f). Although we
517 lose peripheral data, we benefit from the removal of noise in low reflectivity areas around cloud
518 edges, which can develop large values of σ_v^2. The 300-m range resolution of our observations restricts
519 values of Λ_s to multiples of 300 m in order to include whole radial cells, and a minimum of 600 m to
520 include at least two radial cells for the calculation of shear. Under these restrictions, assuming Λ_0 ~
521 1 km, we select Λ_s = 900 m for our observations.

522

5.4 *Variance from azimuthal shear, $\sigma_{s\varphi}^2$*

When RHI or PPI scans are performed, the radial velocity field is observed in two dimensions, the radial direction and the scanning direction. However, these fields include data from three-dimensional sample volumes. In terms of RHIs, Doppler variance from azimuthal shear, $\sigma_{s\varphi}^2$ contributes to σ_v^2, but we are unable to directly estimate it due to scanning in the elevation direction. Unless an adjacent RHI is performed, separated from the first by an angular distance comparable to the width of the beam, S_φ cannot be determined directly. As shown in Section 5.1, variance contributions from $\sigma_{s\varphi}^2$ cannot be ignored in our observations. To account for $\sigma_{s\varphi}^2$ in circumstances where it cannot be measured directly, we investigate statistical relationships between $|S_\varphi|$ and $|S_r|$ derived from PPI radar observations.

PPI scans were performed alongside RHIs scans on DYMECS case days. Doppler velocity fields from PPI scans can be differentiated in the radial and azimuthal directions to determine fields of $|S_\varphi|$ and $|S_r|$. By collecting many co-located pairs of $|S_\varphi|$ and $|S_r|$ from these fields, we attempt to parametrise $|S_\varphi|$ as a function of $|S_r|$. Using the result, $|S_r|$ found in RHIs can be used to estimate $|S_\varphi|$, and its uncertainty, allowing us to account for all components of σ_s^2 in RHI scans.

In order for relationships derived between $|S_\varphi|$ and $|S_r|$ to be of most benefit, we must impose they are calculated over a mutual spatial scale, consistent with that used to calculate $|S_\theta|$ and $|S_r|$ in RHIs, i.e. Λ_s = 900 m. To achieve this, we use a version of (20) tailored to PPI scans, where $S_\theta l_{\theta_i}$ is replaced by $S_\varphi l_{\varphi_i}$, and l_{φ_i} is the azimuthal distance between V_i and V_0. By generating $|S_\varphi|$ and $|S_r|$ values for all V_6 across many PPIs, we could build a dataset consisting of co-located values of $|S_\varphi|$ and $|S_r|$ for statistical assessment.

Figure 2 shows the independent distributions of approximately 10^6 values of S_φ and S_r sourced from 31 PPIs taken on 20 April 2012 at varying elevations. S_φ and S_r are both approximately normally distributed. The combined two-dimensional distribution of S_φ and S_r is circular Gaussian,

approximately centred on $S_r = S_\varphi = 0$. Once the magnitude of the values in the combined distribution is taken, which is the quantity relevant to σ_s^2, $|S_r|$ is divided into contiguous intervals of width 1×10^{-4} s^{-1}. For each of these, we extract the associated dataset of $|S_\varphi|$, and generate its probability density function (PDF). Figure 3 demonstrates that the resulting PDFs are very well approximated by the gamma distribution, given for a random variable x, by (22).

$$\gamma(x|k,l) = \frac{x^{k-1}e^{-\frac{x}{l}}}{\Gamma(k)l^k} \tag{22}$$

Using (22), we can accurately simulate the change in the distribution of $|S_\varphi|$ with $|S_r|$. For each $|S_r|$ interval, we extract the gamma distribution parameters k (shape) and l (scale) from the corresponding distribution of $|S_\varphi|$. By numerically fitting functions to relationships between (k, l) and $|S_r|$, we define k and l in terms of $|S_r|$,

$$k = \begin{cases} |S_r|(A_1|S_r| + A_2) + A_3, & \text{if } |S_r| \leq 0.0017 \text{ s}^{-1} \\ B_1|S_r| + B_2, & \text{otherwise} \end{cases} \tag{23}$$

$$l = C_1|S_r| + C_2 \tag{24}$$

where coefficient values are provided in Table 2. For a given value of $|S_r|$, we use (23) and (24) to produce a PDF of $|S_\varphi|$, and derive our estimate of $|S_\varphi|$ as the mean of this distribution. For a gamma distribution, the mean is simply the product of k and l.

Figure 4 shows the change in median and inter-quartile range (IQR) percentiles of $|S_\varphi|$ with $|S_r|$. Distributions of $|S_\varphi|$ get broader with $|S_r|$. As a result, the size of the IQR, which provides a confidence interval for $|S_\varphi|$, increases with $|S_r|$. The median values of $|S_\varphi|$ increase with $|S_r|$ according to (25) which was obtained by least-squares fitting a quadratic function to the median curve in Figure 4. Mean values of $|S_\varphi|$ also increase with $|S_r|$, with values approximately 25% larger than the median.

$$|S_\varphi|_{\text{med}} = |S_r|(D_1|S_r| + \text{D}_2) + D_3 \tag{25}$$

where coefficient values are provided in Table 2.

Using (23) – (25), $|S_\varphi|$, and an estimate of its uncertainty, can be determined from $|S_r|$ alone. $|S_\varphi|$ is then used in (18) to calculate its variance contribution, $\sigma_{s\varphi}^2$. We can now account for all components of σ_s^2 in (16), subtract σ_s^2 from σ_v^2 to find σ_t^2 using (15), and use σ_t^2 in (2a) and (2b) to determine ε.

5.5 Sensitivity of ε to Λ_s

To perform this sensitivity test, ε is determined in RHI scans of convective clouds using different values of Λ_s in methods to calculate σ_s^2. We use 44 RHI scans performed on 25 August 2012 which provide 3.5×10^5 comparable data points for each Λ_s applied. For all scans, we retrieve $\varepsilon(\Lambda_s)$ where Λ_s is 600 m, 900 m, 1500 m, 2100 m, and 2700 m. As described in Section 5.3, the degree of peripheral data loss in velocity surface fitting increases with Λ_s. To ensure that we are comparing the same data across different Λ_s, the degree of data loss seen when Λ_s = 2700 m has been imposed on all other fields of ε for each scan.

Figure 5 displays the PDFs of $\varepsilon(\Lambda_s)$ using the combined data from all RHIs. It shows that the distribution of ε is largely insensitive to Λ_s, though there is a small increase in the likelihood of low values of ε (less than 0.01 $m^2\ s^{-3}$) with decreased Λ_s. When calculating shear over a smaller Λ_s, the shear magnitude, and therefore σ_s^2, is likely to be higher. This means we remove more of σ_v^2 due to shear, and subsequently derive a lower ε, with the converse true if Λ_s is large. As the change in PDFs of ε is small in Figure 5, we can make rough estimations of Λ_0 (and therefore Λ_s) in the absence of direction measurements, without incurring large errors in ε.

6 Dissipation rate statistics in DYMECS observations

6.1 DYMECS case studies

By applying the methods detailed in Section 2 – 5 across many radar scans, we have performed a statistical assessment of ε in convective storms. We use two contrasting DYMECS days in 2012 as case studies; 20 April (hereafter the "shower" case) and 25 August (hereafter "deep convection" case). In the shower case, low pressure was situated on the east coast of the UK. Convective showers initiated over southern England in the late morning hours, and drifted north-eastwards through the day. In the deep convection case, low pressure was situated over the Irish Sea. Convective storms were more intense and widespread across southern England, with thunderstorms widely reported in the afternoon (Hanley *et al*., 2015). Radar observations were collected using CAMRa in both cases, using a scanning algorithm that prioritised more active convective cells, guided in real time by Met Office network radar observations (Stein *et al*., 2014). As this scanning strategy involved sequential scans of the same cells, a subset of these observations has been taken to include only independent convective storm RHI observations for analysis. This subset consists of 33 RHIs in the shower case, and 44 RHIs for deep convection, however, owing to the 200-km range of CAMRa, multiple convective storms were often present in single RHI scans. In the shower case, these observations show that convection grew to 6 km in height, with updraft vertical velocities w, typically ranging from 1 – 4 m s^{-1}. In the deep convection case, convection grew to 10 km with typical w ranging from 2 – 8 m s^{-1} (Nicol *et al*., 2015).

6.2 Example ε retrievals for convective showers and deep convection

Figures 6 and 7 display examples of retrieved ε for individual convective clouds on the shower and deep convection case days, respectively. These examples have been selected to reflect the typical convective storms observed on each day. Figure 6 depicts a convective shower of 6 km height, with a diffuse updraft region where w is 1 – 3 m s^{-1} (Figure 6c), with a region of strong divergence present in the Doppler velocity above the updraft (Figure 6b). As shown in Figure 6f, ε typically ranges from 0.01 – 0.08 m^2 s^{-3} with the largest values found within the vicinity of the main updraft.

The example of deep convection displayed in Figure 7 has a depth of 10 km, and shows multi-cell characteristics with numerous updraft-downdraft circulations present in Figure 7c. The dominant updraft (~ 34 km from the radar) is narrower and much stronger than for the shower case, with w ranging from 8 – 12 m s^{-1}. Divergence is again apparent in the Doppler velocity towards the upper levels of the cloud (Figure 7b). Figure 7f indicates that turbulence is more intense and widespread than for the shower case, with values of ε typically ranging from 0.03 – 0.3 m^2 s^{-3}. These values are again associated with the main updraft, with the most intense turbulence ($\varepsilon > 0.3$ m^2 s^{-3}) found towards the top of the cloud, above the updraft.

In many of the cloud cases that were examined to derive the statistics of ε presented later in this section, values of σ_s^2 were small compared to σ_t^2 and largely remained below σ_{neg}^2. The retrievals presented in Figures 6 and 7 provide examples of this; values of $\sigma_s^2 > \sigma_{neg}^2$ were absent in the shower cloud and were restricted to a small cluster of 36 pulse volumes in the deep cloud case. This region is evident in Figure 7e, located from 7.5 – 8 km in height at an approximate range of 33 – 34 km. Although σ_s^2 was significant in this region, values remained less than 15% of σ_t^2 suggesting that σ_s^2 could have been neglected in these two cloud examples without significantly over-estimating ε.

Shear corrections are, however, not negligible for all cloud cases considered, especially for those located further from the radar. According to (17) and (18), variances from azimuthal and elevation shear components increase with range squared. Figure 8 presents the ratio of σ_s^2 to σ_t^2 in an example cloud observed between 90 – 115 km from the radar on 20 April 2012. Within the region of $\sigma_s^2 > \sigma_{neg}^2$ (black contour) values of σ_s^2 vary between 30% – 70% of σ_t^2. Neglecting σ_s^2 in this region would result in the over-estimation of mean ε by 52%. Given that clouds were commonly observed 100 km (or further) from the radar, Figure 8 provides an example of the requirement to remove σ_s^2 in our data to ensure accurate retrievals of ε.

By inspecting many retrievals of ε in convective clouds across two contrasting days of convection, the rest of this section is focused on relating ε to convective storm characteristics in a statistical sense.

642

643 *6.3 Vertical distribution of ε in convective clouds*

644 Statistics have been collected for ε in vertical layers of 1-km depth from the subsets of RHI
645 observations described in Section 6.1. Using this approach, we can assess the vertical distribution of
646 ε in convective clouds (where $Z > -20$ dBZ), and see how this differs for showers and deep
647 convection.

648 Figure 9 shows how the median, and 25th, 75th and 95th percentiles of ε change with height in the
649 cloud; 0 – 6 km for showers, 0 – 10 km for deep convection. For showers and deep convection, the
650 95th percentiles of ε (hereafter ε_{95}) from 0 – 1 km are approximately the same, at ~ 0.025 $m^2\ s^{-3}$.
651 For the shower case, this remains approximately constant with height, varying between 0.02 – 0.03
652 $m^2\ s^{-3}$ and peaking at a height of 5 km. For deep convection, ε_{95} increases significantly with height,
653 becoming twice as large as for the shower case at 6 km height (0.05 $m^2\ s^{-3}$), and increasing to 0.1
654 $m^2\ s^{-3}$ at 10 km height. The median ε is an approximately constant 0.01 $m^2\ s^{-3}$ throughout the 6-
655 km depth of the shower cases. For the same depth of deep convective cloud, the median is almost
656 identical to the shower case, and then increases from 0.01 – 0.03 $m^2\ s^{-3}$ from 6 – 10 km.

657 The 25th and 75th percentiles of ε follow a very similar pattern to this, indicating that from 0 – 6
658 km the average intensity of turbulence is very similar for both cases. The reason for this is highlighted
659 by Figure 6f and 7f; turbulence is locally intense, but a large proportion of the cloud area is only
660 weakly turbulent in both cases ($\varepsilon \leq 0.01\ m^2\ s^{-3}$). This was often the case throughout observations
661 on both days which serves to explain why the bulk of ε values are so similar. Where the cloud is
662 turbulent however, values of ε are much larger in deep convection with much stronger circulations,
663 which is reflected in the notable difference in ε_{95} between the two cases.

664

665 *6.4 ε in convective updraft regions*

As we are most interested in the turbulent regions of individual convective clouds, and turbulence in observations tends to be associated with convective updrafts (see Figures 6 and 7), we refine this investigation to ε located only in convective updraft regions.

The following method has been selected in part to ensure it can be applied identically to numerical model data in future investigations. To detect coherent updraft regions, a flood-fill algorithm is applied to vertical cross-sections of w (T. Stein, personal communication), to automatically detect contiguous regions with w above specified thresholds, and record their co-ordinates. By taking the four spatial extremes of these co-ordinates, a box is drawn around an updraft – defined as an updraft *region*. Updrafts are often irregular in shape in observations, so this approach includes some data surrounding the updraft in the defined region. As a result, we benefit from including some information about turbulence associated with an updraft, without it having to be co-located with specific values of w.

Once updraft regions are defined, they are filtered by width and depth to avoid the inclusion of very small, insignificant updrafts that are detected by the algorithm. For the shower case, we used a minimum threshold w of 1 m s^{-1}, and a minimum depth of 2 km. For the deep convection case, we used a minimum threshold w of 1.5 m s^{-1}, and a minimum depth of 3 km. In both cases, a minimum updraft region width of 1.5 km was imposed. The lower thresholds for w and depth used in the shower case were chosen due to the weaker, shallower updrafts observed on that day. Using this approach, 77 updraft regions were detected in the shower case, and 101 regions for deep convection. The co-ordinates of each region can then be super-imposed on fields of ε for analysis.

Figure 10 displays scatter plots relating ε_{95} for each updraft region to its (a) 95th percentile of w (hereafter w_{95}), (b) 95th percentile of the magnitude of the horizontal gradient in w, $\left|\frac{dw}{dx}\right|_{95}$, (c) updraft width, and (d) updraft depth. In Figure 10a, we see that ε_{95} has a significant ($p < 10^{-3}$) positive correlation with w_{95} for both showers ($r = 0.425$) and deep convection ($r = 0.594$). Correlations with $\left|\frac{dw}{dx}\right|_{95}$ (Figure 10b) are marginally stronger than with w_{95} ($r = 0.517$ for showers, $r = 0.671$

for deep convection). This suggests that strong gradients in w are more important in generating turbulence than w alone. Weaker positive correlations exist between ε_{95} and the width and depth of updrafts for both showers ($r = 0.295$ for width, and $r = 0.314$ for depth), and deep convection ($r = 0.309$ for width, and $r = 0.390$ for depth). This indicates that the intensity of turbulence is not highly sensitive to the dimensions of the updraft. The consistency of correlations between the two cases, albeit with a smaller range in variable values for the shower case, suggests that these relationships may not be restricted to individual cases, or days of observation.

To produce Figure 11, all ε values in an updraft region are added to a distribution based on w_{95}. By doing this, we can assess how the full distribution of ε changes with w_{95} in the two cloud types, instead of just the largest values. These distributions are displayed in the form of cumulative density functions (CDFs) for every 2 m s^{-1} interval in w_{95}. In both the showers and deep convection, a trend towards a lower probability of small ε, and a higher probability of large ε is seen with w_{95}. In both cases, small values of ε (less than 0.01 m^2 s^{-3}) are approximately twice as likely to appear in updrafts with $w_{95} < 4$ m s^{-1}, than for those $w_{95} > 4$ m s^{-1}. In the shower case, ε larger than 0.05 m^2 s^{-3} has a probability of less than 0.01 in all updraft regions ($w_{95} < 6$ m s^{-1}); whereas for the same w_{95} intervals of deep convection the probability is as large as 0.12. This indicates that stronger turbulence is more likely to be found in deep convective clouds than for showers of the same updraft strength. However, we see only a snapshot of information for each convective cloud; turbulent energy will take time to reach dissipation scales, in which time updrafts could have weakened considerably. The probability of large values of ε (more than 0.1 m^2 s^{-3}) is 0 for the shower case, but as high as 0.05 for deep convection. When w_{95} is 2 – 4 m s^{-1}, the CDFs of ε are very similar for both cases, further indicating that ε may be a function of storm characteristics independent of case, or day of observation.

7 Summary and Conclusions

715 A comprehensive analysis of processes contributing to the width of the Doppler velocity spectrum
716 has been performed, with the objective of developing a rigorous algorithm to estimate turbulence
717 intensity expressed as a dissipation rate.

718 New equations to quantify the spectral broadening effect due to a distribution of hydrometeor fall
719 speeds (σ^2_{TV}) have been presented for ice aggregates, raindrops and hail. We conclude that $\sigma^2_{\mathrm{TV_{agg}}}$ is
720 always negligibly small, and $\sigma^2_{\mathrm{TV_{rain}}}$ and $\sigma^2_{\mathrm{TV_{hail}}}$ are negligible when observing at elevations lower
721 than 13.9° and 11.5°, respectively. We find that σ^2_{TV} can be larger than 8 $\mathrm{m^2\ s^{-2}}$ if scanning vertically
722 through heavy rain or hail, and recommend avoiding high-elevation scanning when attempting to
723 retrieve turbulence from the spectrum width.

724 Methods have been presented to remove contributions to σ_v^2 from shear over scales larger than
725 those sampled by the radar. This was achieved by evaluating shear over a constant spatial scale (Λ_s),
726 using linear velocity surface fitting techniques as employed in past studies. Resulting values of ε
727 have been found to be insensitive to Λ_s. To permit the estimation of ε from σ_{t}^2, it is of key importance
728 that the largest dimension of V_6 is lower than Λ_0.

729 To account for spectrum width contributions from shear in the azimuthal direction, we have
730 derived a new equation for the median azimuthal shear as a function of radial shear alone. This can
731 be used to account for 3-D shear broadening in 2-D radar scans, and can be used simply to further
732 improve the accuracy of retrieved ε. After noting incorrect equations for the calculation of σ_s^2 in the
733 literature, we conclude the correct equations are those derived in Appendix S1.

734 By applying the retrieval method across many observations on two contrasting DYMECS case
735 days, we have produced statistics of ε in convective clouds. Turbulence is generally much stronger
736 in deep convective cloud (0.03 – 0.3 $\mathrm{m^2\ s^{-3}}$) than in shower cloud (0.01 – 0.08 $\mathrm{m^2\ s^{-3}}$). In both
737 cases, the majority of cloud is generally weakly turbulent, with significant turbulence co-located
738 with, but not limited to, areas of shear and buoyancy. Strong turbulence is more widespread towards
739 the top of deep convective cloud, while vertical profiles of turbulence are approximately constant in

740 shower cloud. In updraft regions, turbulence is strongly correlated with updraft strength, and there is
741 evidence that gradients in the vertical velocity are more important in generating strong turbulence
742 than the updraft velocity alone. Turbulence is only weakly correlated with the spatial dimensions of
743 updrafts.

744 Our method has sourced, developed, and added to many decades of turbulence retrieval research
745 to form the most comprehensive approach to date. Though we have ultimately applied the method to
746 a specific radar and observational dataset, the considerations made in Sections 2 – 5 are suitably
747 general, forming a reliable framework for turbulence retrieval with other high-resolution radars
748 capable of sampling inertial sub-range turbulence.

749 Following directly from this research, we have collected new observations of convective clouds
750 with CAMRa, under an improved scanning strategy better suited to turbulence retrieval. By
751 performing multiple RHI scans separated by small azimuthal distances across clouds, we aim to
752 investigate the 3-D structures of turbulence in convective storms.

753 We have also used the results of this investigation to evaluate the performance of the
754 Smagorinsky-Lilly sub-grid scheme through direct comparisons with ε in high-resolution NWP
755 simulations of the observed cases. The degree to which our observations can be used more generally
756 to evaluate turbulence characteristics in CPMs (without the need to simulate the observed cases) is
757 not clear. However, at the very least, our observations can provide guidance for the typical
758 characteristics of ε in clouds for comparison with other high-resolution CPM simulations, given that
759 ε can be found as a diagnostic output from the turbulence parametrisation. To ultimately improve the
760 versatility of our results, we aim to extend our observations to more diverse cloud cases to assess the
761 degree to which our statistics are case-dependent.

762

763 **Acknowledgements**

764 This research was conducted with funding from the Natural Environment Research Council
765 (NERC) under the SCENARIO programme. Acknowledgements go to Dr. John Nicol in providing
766 vertical velocity retrievals for the case studies investigated, which have been invaluable to the
767 analysis of turbulence in convective clouds. Further thanks go to staff at the Chilbolton Observatory
768 for the technical support with data from CAMRa.

769

770 **Supporting information:**

771 **Appendix S1 – Derivation of spectral variance equations for shear**

772

773 REFERENCES

774 Albrecht BA, Fang M, Ghate VP. 2016. Exploring stratocumulus cloud-top entrainments processes
775 and parameterizations by using Doppler cloud radar observations. *J. Atmos. Sci.*, **54**: 729-742.
776 Atlas D, Ulbricht CW. 1977. Path- and area-integrated rainfall measurement by microwave
777 attenuation in the 1-3 cm band. *J. Appl. Meteorol.* **16**: 1322–1331.
778 Battan LJ. 1975. Doppler radar observations of a hailstorm. *J. Appl. Meteorol.* **14**: 98-108.
779 Blyth AM, Cooper AC, Jensen JB. 1988. A study of the source of entrained air in Montana Cumuli.
780 *J. Atmos. Sci.* **45**: 3944-3964.
781 Blyth AM. 1993. Entrainment in cumulus clouds. *J. Appl. Meteorol.* **32**: 626-641.
782 Bouniol D, Illingworth AJ, Hogan RJ. 2003. Deriving turbulent kinetic energy dissipation rate within
783 clouds using ground based 94 GHz radar. Preprints, 31st Conf. on Radar Meteorology, Seattle,
784 WA, Amer. Meteor. Soc. 192-196.
785 Brewster KA, Zrnic DS. 1986. Comparison of eddy dissipation rates from spatial spectra of Doppler
786 velocities and Doppler spectrum widths. *J. Atmos. Oceanic Technol*. **3**: 440-552.

787 Chapman D, Browning KA. 2001. Measurements of dissipation rate in frontal zones. *Q. J. R.*
788 *Meteorol. Soc*. **127**: 1939-1959.
789 Cheng L, English M. 1982. A relationship between hailstone concentration and size. *J. Atmos. Sci.*
790 **40**: 204-213.
791 Clark P, Roberts N, Lean H, Ballard SP, Charlton-Perez C. 2016. Convection-permitting models: a
792 step-change in rainfall forecasting. *Meteorol. Appl.* **23**: 165-181.
793 Cox GP. 1988. Modelling precipitation in frontal rainbands. *Q. J. R. Meteorol. Soc.* **114**: 115–127.
794 Depue TK, Kennedy PC, Rutledge SA. 2007. Performance of the hail differential reflectivity (H_{DR})
795 polarimetric radar hail indicator. *J. Appl. Meteorol. Climatol.* **46**: 1290-1301.
796 Doviak RJ, Zrnic DS. 1984. Doppler radar and weather observations. *Academic Press.*
797 Falkovich G, Fouxon A, Stepanov MG. 2002. Acceleration of rain initiation by cloud turbulence.
798 *Nature*. **419**: 151-154.
799 Fang M, Albrecht BA, Ghate VP, Kollias P. 2014. Turbulence in continental stratocumulus, part II:
800 Eddy dissipation rates and large-eddy coherent structures. *Bound.-Layer Meteor.*, **150**: 361-380.
801 Frisch AS, Clifford SF. 1974. A Study of Convection Capped by a Stable Layer Using Doppler Radar
802 and Acoustic Echo Sounders. *J. Atmos. Sci.* **31**: 1622–1628.
803 Grover SN, Pruppacher HR. 1985. The effect of vertical turbulent fluctuations in the atmosphere on
804 the collection of aerosol particles by cloud drops. *J. Atmos. Sci.* **42**: 2305-2318.
805 Gunn KLS, Marshall RS. 1958. The distribution of size of aggregate snowflakes. *J. Meteorol. Soc.*
806 **80**: 522-545.
807 Hanley KE, Plant RS, Stein THM, Hogan RJ, Nicol JC, Lean HW, Halliwell CE, Clark PA. 2015.
808 Mixing length controls on high resolution simulations of convective storms. *Q. J. R. Meteorol.*
809 *Soc*. **141**: 272-284.
810 Istok MJ, Doviak RJ. 1986. Analysis of the relation between Doppler spectral width and thunderstorm
811 turbulence. *J. Atmos. Sci.* **43**: 2199-2214.
812 Keeler JR, Passarelli RE. 1990. Signal processing for atmospheric radars. *Radar in Meteorology*.

DOI 10.1007/978-1-935704-15-7_21. 199-229.

Khain AP, Pinsky MB. 1995. Drops' inertia and its contribution to turbulent coalescence in convective clouds: Part 1. Drops' fall in the flow with random horizontal velocity. *J. Atmos. Sci.* **52**: 196-206.

Knupp KR, Cotton WR. 1982. An intense, quasi-steady thunderstorm over mountainous terrain, part III: Doppler radar observations of the turbulent structure. *J. Atoms. Sci.* **39**: 359-368.

Labitt, M. 1981. Co-ordinated radar and aircraft observations of turbulence. Project Rep. ATC 108, MIT, Lincoln Lab, 39 pp.

Lhermitte RM. 1963. Motions of scatterers and the variance of the mean intensity of weather radar signals. SRRC-RR-63-57. Sperry-Rand Res. Cent., Sudbury, Massachusetts.

Marshall JS, Palmer WM. 1948. The distribution of raindrops with size. *J. Meteorol.* **5**: 165-166.

Meishner P, Baumann R, Holler H, Jank T. 2001. Eddy dissipation rates in thunderstorms estimated by Doppler radar in relation to aircraft in-situ measurements. *J. Atmos. Oceanic. Technol*. **18**: 1609-1627.

Melnikov VM, Doviak RJ. 2009. Turbulence and wind shear in layers of large Doppler spectrum width in stratiform precipitation. *J. Atmos. Oceanic Technol*. **26**: 430-443.

Neter J, Wasserman W. 1974. Applied linear statistical models, 842pp.

Nicol JC, Hogan RJ, Stein THM, Hanley KE, Clark PA, Halliwell CE, Lean HW, Plant RS. 2015. Convective updraft evaluation in high-resolution NWP simulations using single-Doppler measurements. *Q. J. R. Meteorol. Soc.* **141**: 3177-3189.

Pinksy MB, Khain AP. 2002. Effects of in-cloud nucleation and turbulence on droplet spectrum formation in cumulus clouds. *Q. J. R. Meteorol. Soc.* **128**: 501-533.

Pruppacher HR, Klett JD. 1978. Microphysics of clouds and precipitation. D. Reidel Publishers, Dordrecht, 714pp.

Shupe MD, Brooks IM, Canut G. 2012. Evaluation of turbulent dissipation rate retrievals from Doppler cloud radar. *Atmos. Meas. Tech.* **5**: 1375-1385.

839 Stein THM, Hogan RJ, Clark PA, Halliwell CE, Hanley KE, Lean HW, Nicol JC, Plant RS. 2015.
840 The DYMECS Project: A statistical approach for the evaluation of convective storms in high-
841 resolution NWP models. *Bull. Amer. Meteor. Soc.* **96**: 939-951.
842 Ulbricht CW. 1974. Analysis of Doppler radar spectra of hail. *J. Appl. Meteorol.* **13**: 387-396.
843 Vohl O, Mitra SK, Wurzler SC, Pruppacher HR. 1999. A wind tunnel study of the effects of
844 turbulence on the growth of cloud droplets by collision and coalescence. *J. Atmos. Sci.* **56**: 4088-
845 4099.
846 Waldvogel A, Schmidt W, Federer B. 1978. The kinetic energy of hailfalls. Part I: Hailstone spectra.
847 *J. Appl. Meteorol.* **17**: 515-520.
848 Zrnic DS, Doviak RJ, 1989. Effect of drop oscillations on spectral moments and differential
849 reflectivity measurements. *J. Atmos. Oceanic Technol*. **6**: 532-536.

850

851

852 **Figure Captions**

853

854 **Figure 1.** (a) Change in $\sigma^2_{\mathrm{TV}_j}$ for rain, ice aggregates and hail, with radar reflectivity Z_j, and elevation
855 angle, θ_{el}. Black lines refer to observations made at vertical incidence; grey lines at $\theta_{\mathrm{el}} = 15°$. (b)
856 The impact on $\sigma^2_{\mathrm{TV}_{\mathrm{hail}}}$ of using different $V_{\mathrm{hail}}(D)$ relationships in the derivation of (13); (1) $p =$
857 142.6, $q = 0.5$, (2) $p = 162.0$, $q = 0.5$, (3) $p = 359.0$, $q = 0.8$. Results are displayed for $\sigma^2_{\mathrm{TV}_{\mathrm{hail}}}$
858 sampled at vertical incidence ($\theta_{\mathrm{el}} = 90°$). (c) The change in $\sigma^2_{s\theta}$, $\sigma^2_{s\varphi}$ and σ^2_{sr} (Eq. (17) – (19)) with
859 shear magnitude, $|S|$. Variances $\sigma^2_{s\theta}$, and $\sigma^2_{s\varphi}$ are displayed for ranges 30 km and 150 km, which are
860 roughly the minimum and maximum ranges of radar observations in the DYMECS data. Shears larger
861 than 0.02 s^{-1} were uncommon in our observations. In each panel, the threshold for negligibility σ^2_{neg},
862 is plotted for reference as a dashed line at 0.5 $\mathrm{m}^2\mathrm{s}^{-2}$.

863

Figure 2. Independent distributions of 1×10^6 values of S_φ and S_r sourced from 31 PPI scans performed on 20 April 2012.

Figure 3. Change in the PDFs of observed $|S_\varphi|$ for three selected intervals of $|S_r|$ (solid lines). Distributions of $|S_\varphi|$ are well approximated by Gamma PDFs (22) (dashed lines). The width of each $|S_r|$ interval is 1×10^{-4} s^{-1}, and the interval of $|S_r|$ for each distribution is displayed in the figure titles.

Figure 4. The change in the median, 25th and 75th percentile values of $|S_\varphi|$ with $|S_r|$.

Figure 5. The insensitivity of distributions of ε to the scale Λ_s, over which shear is calculated for σ_s^2.

Figure 6. Example ε retrieval for an RHI scan of a convective storm performed on the 20 April 2012 (showers). Included is (a) radar reflectivity, (b) Doppler velocity, (c) vertical velocity, (d) total Doppler variance, (e) Doppler variance due to shear, and (f) eddy dissipation rate displayed in $\log_{10}$ units. The grey contour outlines reflectivity returns of -20 dBZ.

Figure 7. Equivalent to Figure 6, an example retrieval of ε for an RHI scan of a convective storm performed on the 25 August 2012 (deep convection).

Figure 8. The ratio of shear (σ_s^2) and turbulent (σ_t^2) contributions to Doppler variance in an example shower cloud observed on 20 April 2012. The location of values of σ_s^2 that exceed σ_{neg}^2 is indicated by the black contour. In this example, neglecting σ_s^2 in the contoured region results in the considerable over-estimation of mean ε by 52%.

Figure 9. Comparison of the vertical distribution of various percentiles of ε in convective clouds ($Z > -20$ dBZ) on 20 April (showers) and 25 August (deep convection), 2012. Percentiles for each 1 km layer are plotted at the midpoint of that layer.

Figure 10. Scatter plots comparing the 95th percentile of ε for each updraft region ε_{95}, on 20 April (showers) and 25 August (deep convection), 2012, to the following corresponding statistics: (a) the 95th percentile of vertical velocity w_{95}, (b) the 95th percentile of the magnitude of the horizontal gradient in vertical velocity $\left|\frac{dw}{dx}\right|_{95}$, (c) the updraft width, and (d) the updraft depth.

Figure 11. The change in the cumulative density function (CDF) of ε in updraft regions with different 95th percentile values of w (w_{95}) for 20 April 2012 shower updrafts (black lines) and 25 August 2012 deep updrafts (grey lines). Values of w_{95} did not exceed 6 m s^{-1} in any shower updraft region. Values of w_{95} smaller than 2 m s^{-1} were not found in any deep updraft region.

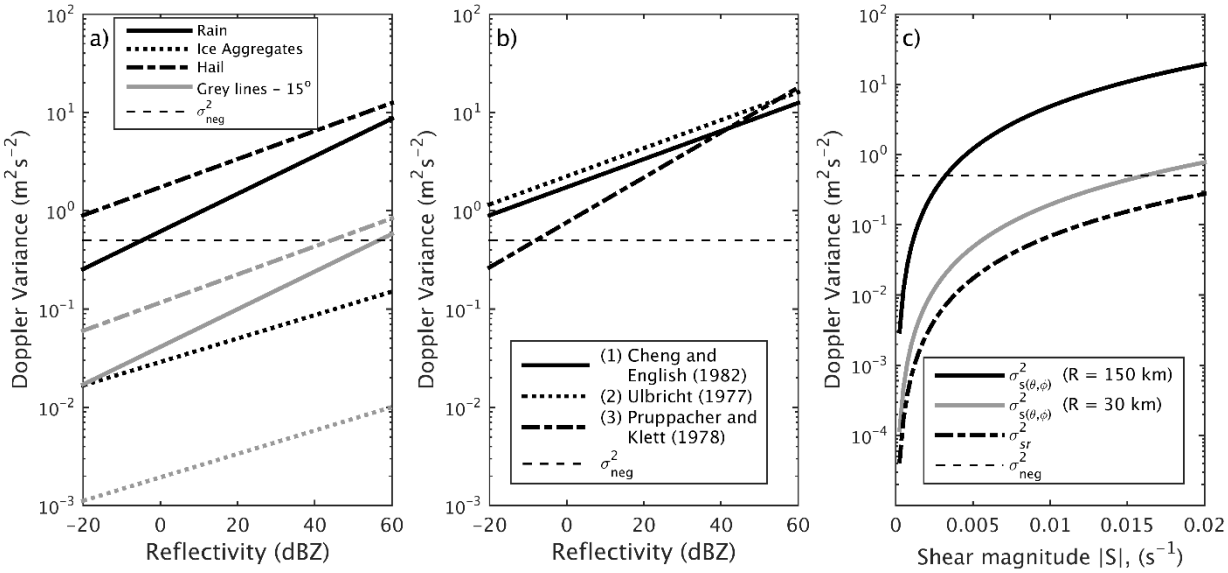
a)
Rain
Ice Aggregates
Hail
Grey lines – 15°
σ^2_{neg}
Doppler Variance ($m^2 s^{-2}$)
Reflectivity (dBZ)
b)
(1) Cheng and English (1982)
(2) Ulbricht (1977)
(3) Pruppacher and Klett (1978)
σ^2_{neg}
Doppler Variance ($m^2 s^{-2}$)
Reflectivity (dBZ)
c)
$\sigma^2_{s(\theta,\phi)}$ (R = 150 km)
$\sigma^2_{s(\theta,\phi)}$ (R = 30 km)
σ^2_{sr}
σ^2_{neg}
Doppler Variance ($m^2 s^{-2}$)
Shear magnitude |S|, (s^{-1})

Figure 1

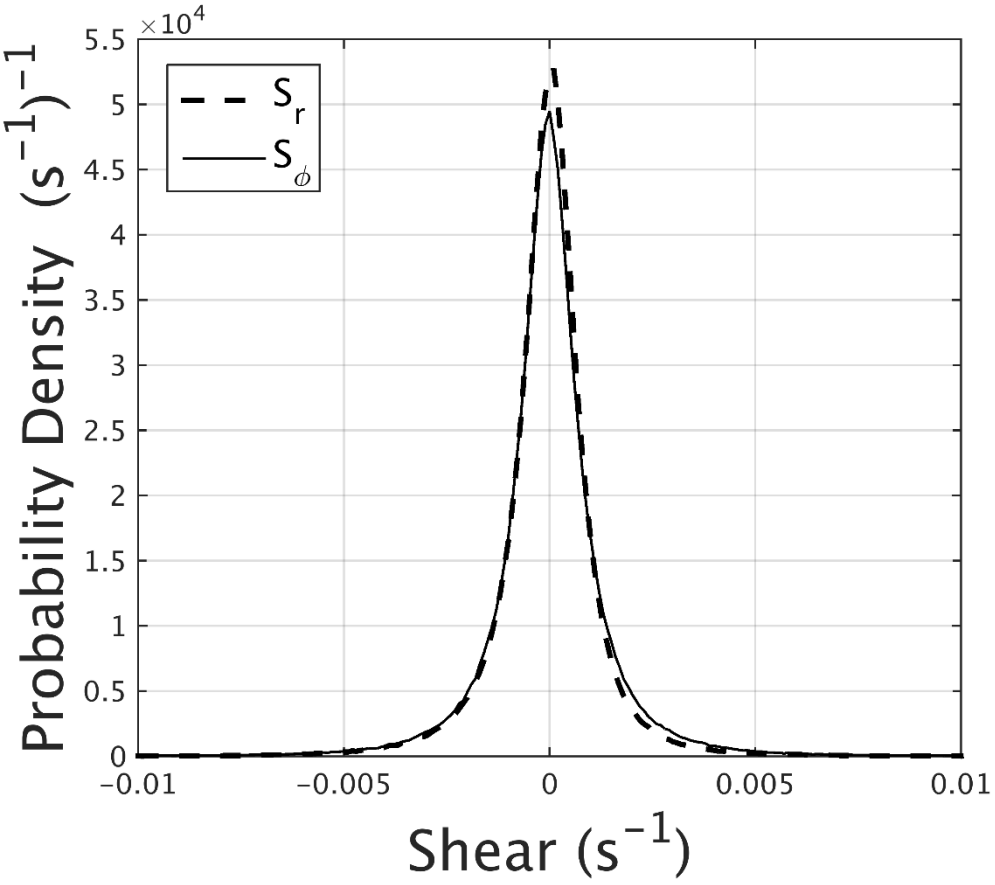
×10^4
5.5
5
4.5
4
3.5
3
2.5
2
1.5
1
0.5
0
Probability Density (s^-1)^-1
S_r
S_φ
−0.01
−0.005
0
0.005
0.01
Shear (s^-1)

Figure 2

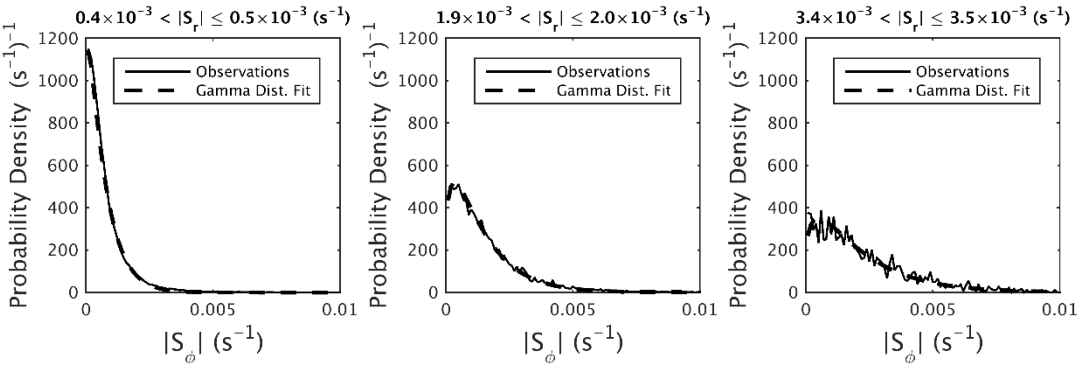
$0.4\times10^{-3} < |S_r| \leq 0.5\times10^{-3}$ (s^{-1})
$1.9\times10^{-3} < |S_r| \leq 2.0\times10^{-3}$ (s^{-1})
$3.4\times10^{-3} < |S_r| \leq 3.5\times10^{-3}$ (s^{-1})
Observations
Gamma Dist. Fit
Probability Density $(s^{-1})^{-1}$
$|S_\phi|$ (s^{-1})
0
200
400
600
800
1000
1200
0.005
0.01

Figure 3

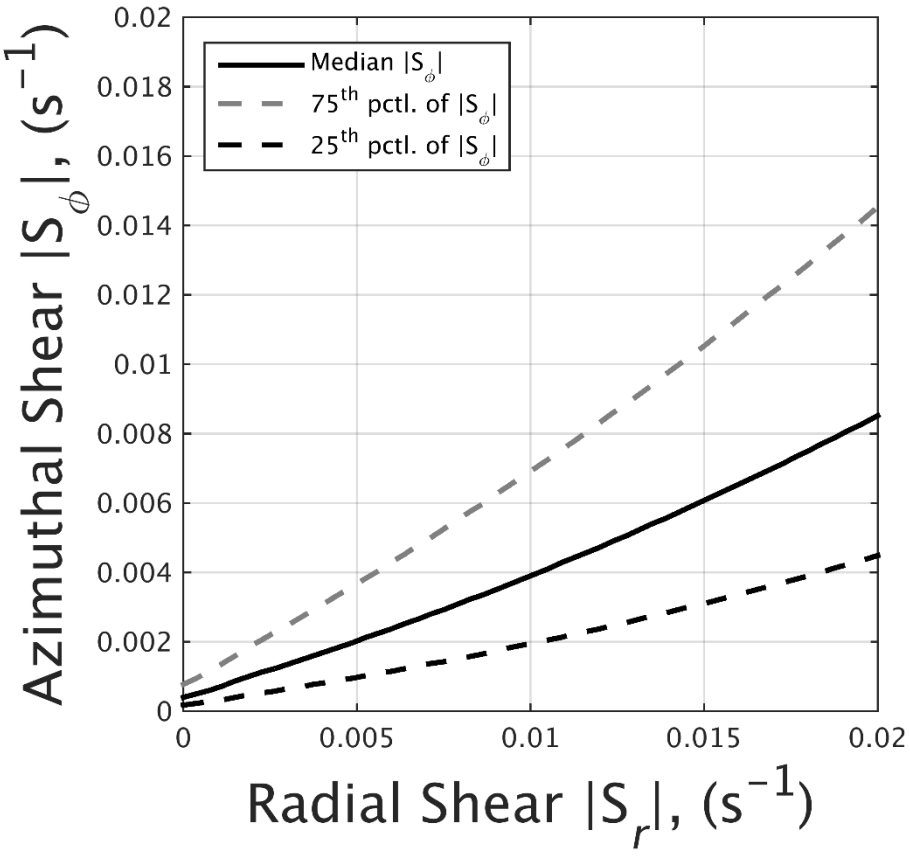
Median $|S_\phi|$
75^{th} pctl. of $|S_\phi|$
25^{th} pctl. of $|S_\phi|$
Azimuthal Shear $|S_\phi|$, (s^{-1})
Radial Shear $|S_r|$, (s^{-1})
0
0.002
0.004
0.006
0.008
0.01
0.012
0.014
0.016
0.018
0.02
0.005
0.015

Figure 4

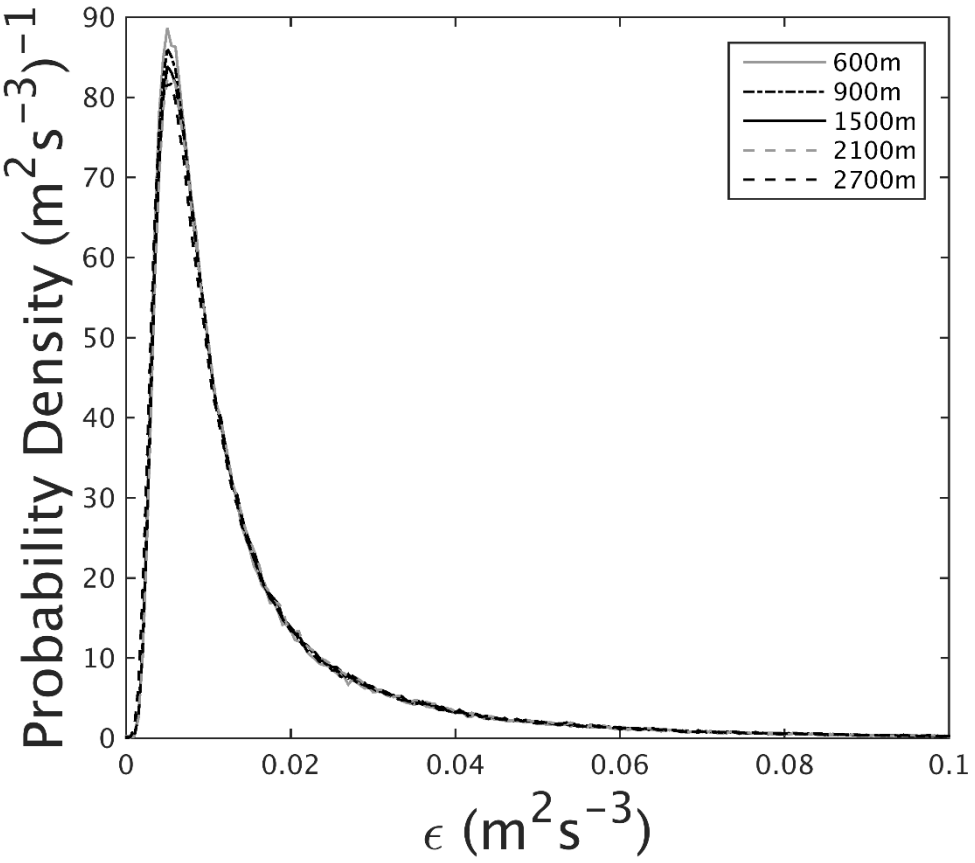
Probability Density (m^2s^{-3})$^{-1}$
ϵ (m^2s^{-3})
0
10
20
30
40
50
60
70
80
90
0
0.02
0.04
0.06
0.08
0.1
600m
900m
1500m
2100m
2700m

Figure 5

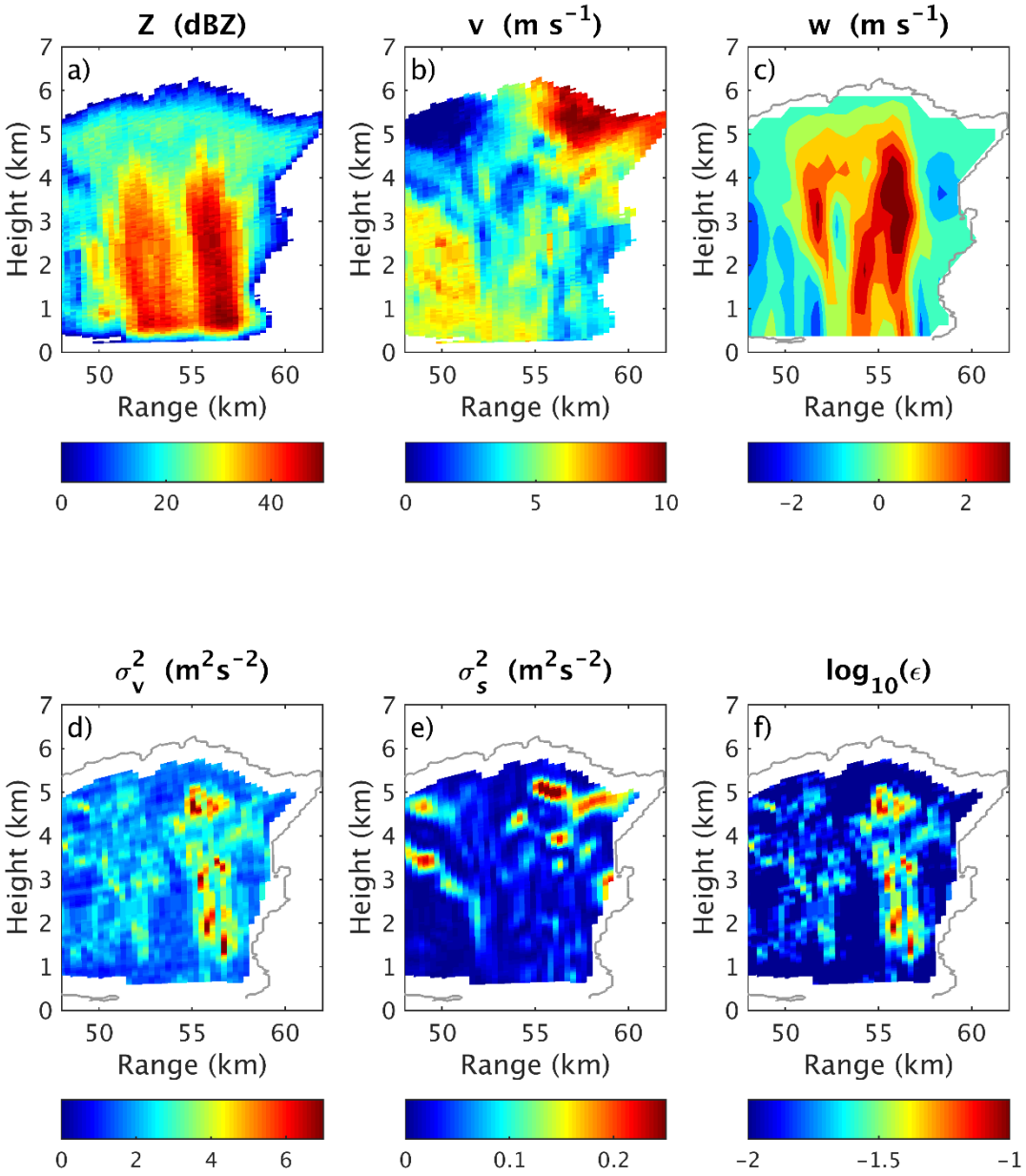
Z (dBZ)
v (m s^{-1})
w (m s^{-1})
a)
b)
c)
Height (km)
Range (km)
0 20 40
0 5 10
−2 0 2
σ_v^2 (m^{2}s^{-2})
σ_s^2 (m^{2}s^{-2})
log$_{10}(\epsilon)$
d)
e)
f)
0 2 4 6
0 0.1 0.2
−2 −1.5 −1

Figure 6

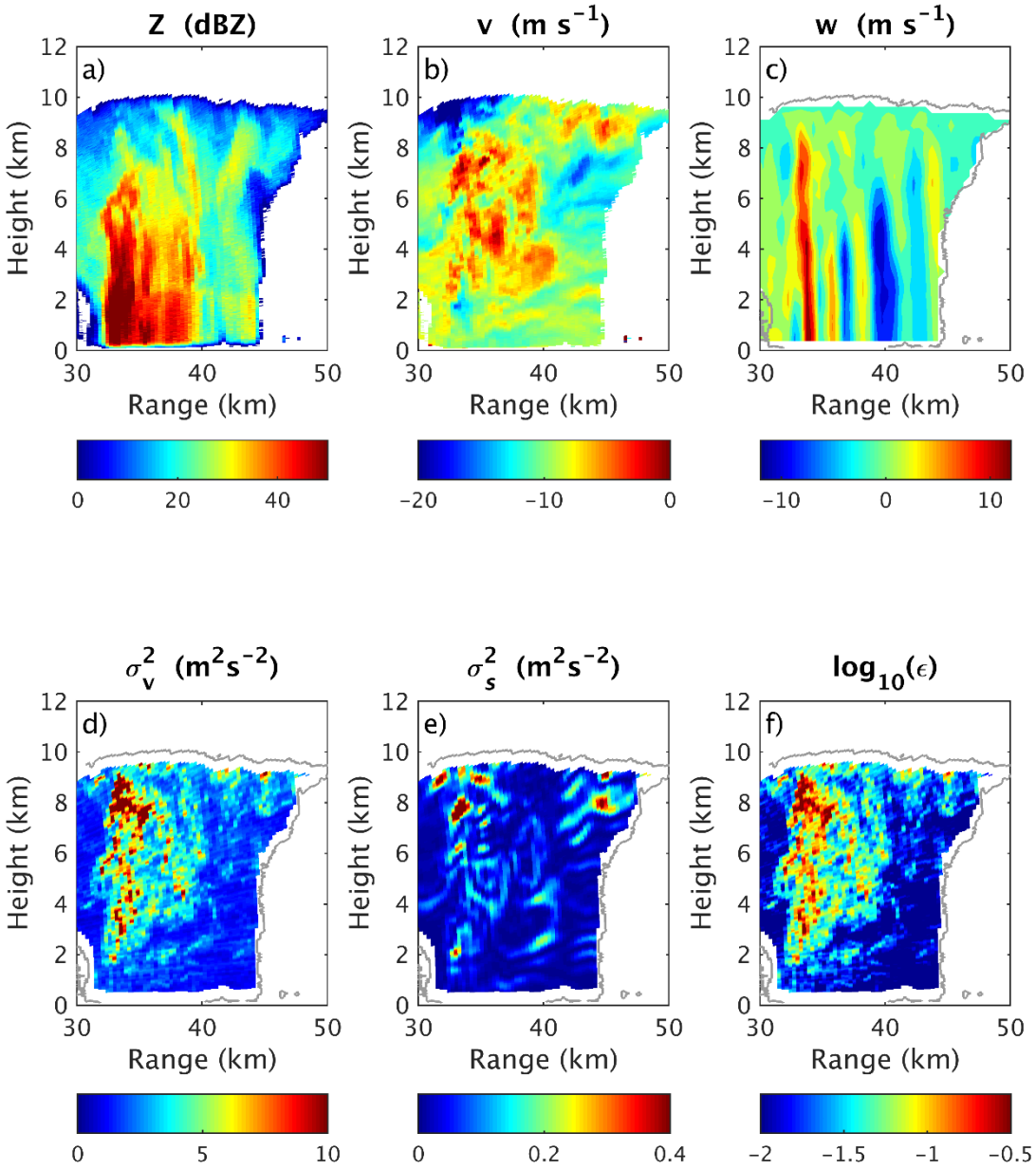
Z (dBZ)
v (m s^{-1})
w (m s^{-1})
a)
b)
c)
d)
e)
f)
Height (km)
Range (km)
σ_v^2 (m^{2}s^{-2})
σ_s^2 (m^{2}s^{-2})
log$_{10}(\epsilon)$

Figure 7

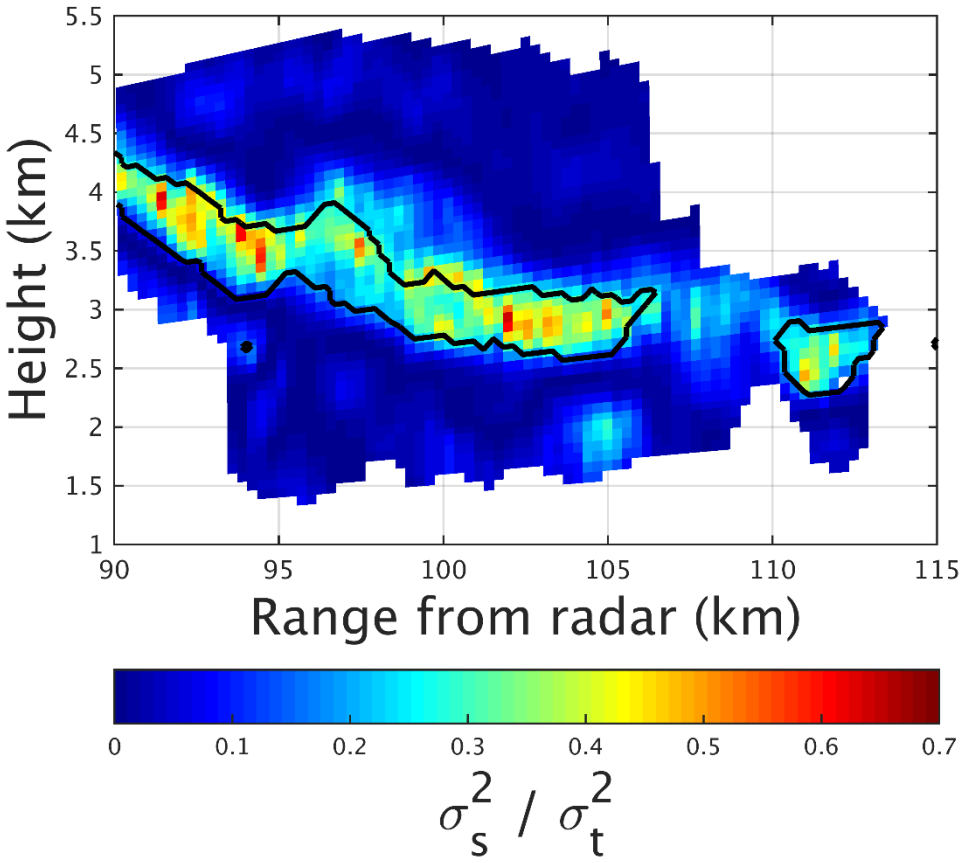
Height (km)
5.5
5
4.5
4
3.5
3
2.5
2
1.5
1
90
95
100
105
110
115
Range from radar (km)
0
0.1
0.2
0.3
0.4
0.5
0.6
0.7
σ_s^2 / σ_t^2

Figure 8

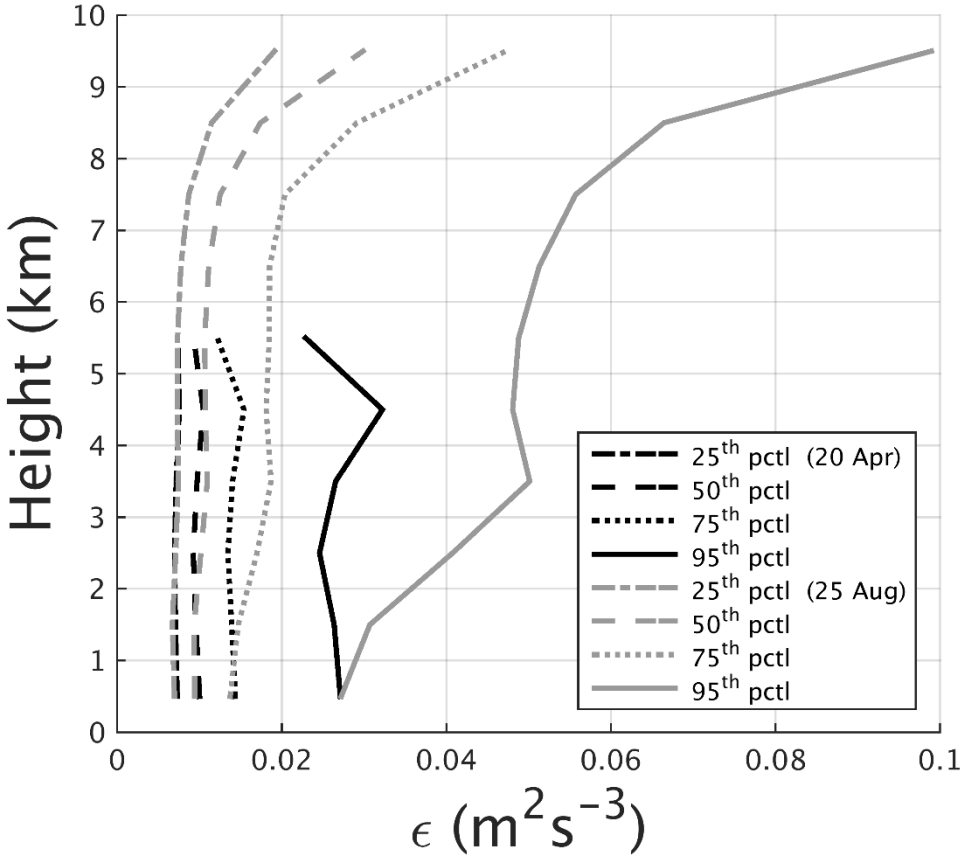
Height (km)
ϵ (m^2s^{-3})
25th pctl (20 Apr)
50th pctl
75th pctl
95th pctl
25th pctl (25 Aug)
50th pctl
75th pctl
95th pctl

Figure 9

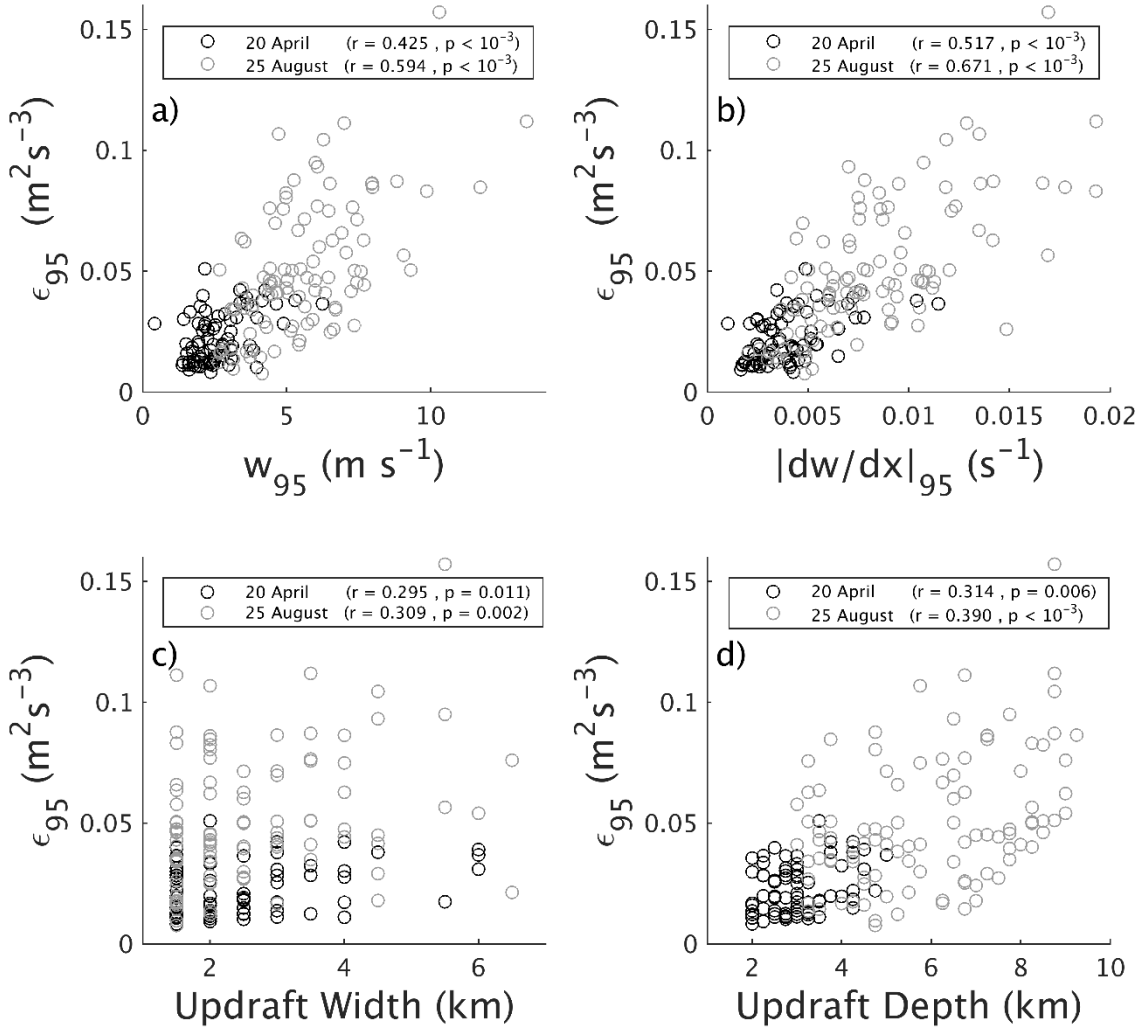
a)
20 April (r = 0.425 , p < 10^-3)
25 August (r = 0.594 , p < 10^-3)
ϵ95 (m2s-3)
w95 (m s-1)
b)
20 April (r = 0.517 , p < 10^-3)
25 August (r = 0.671 , p < 10^-3)
ϵ95 (m2s-3)
|dw/dx|95 (s-1)
c)
20 April (r = 0.295 , p = 0.011)
25 August (r = 0.309 , p = 0.002)
ϵ95 (m2s-3)
Updraft Width (km)
d)
20 April (r = 0.314 , p = 0.006)
25 August (r = 0.390 , p < 10^-3)
ϵ95 (m2s-3)
Updraft Depth (km)

Figure 10

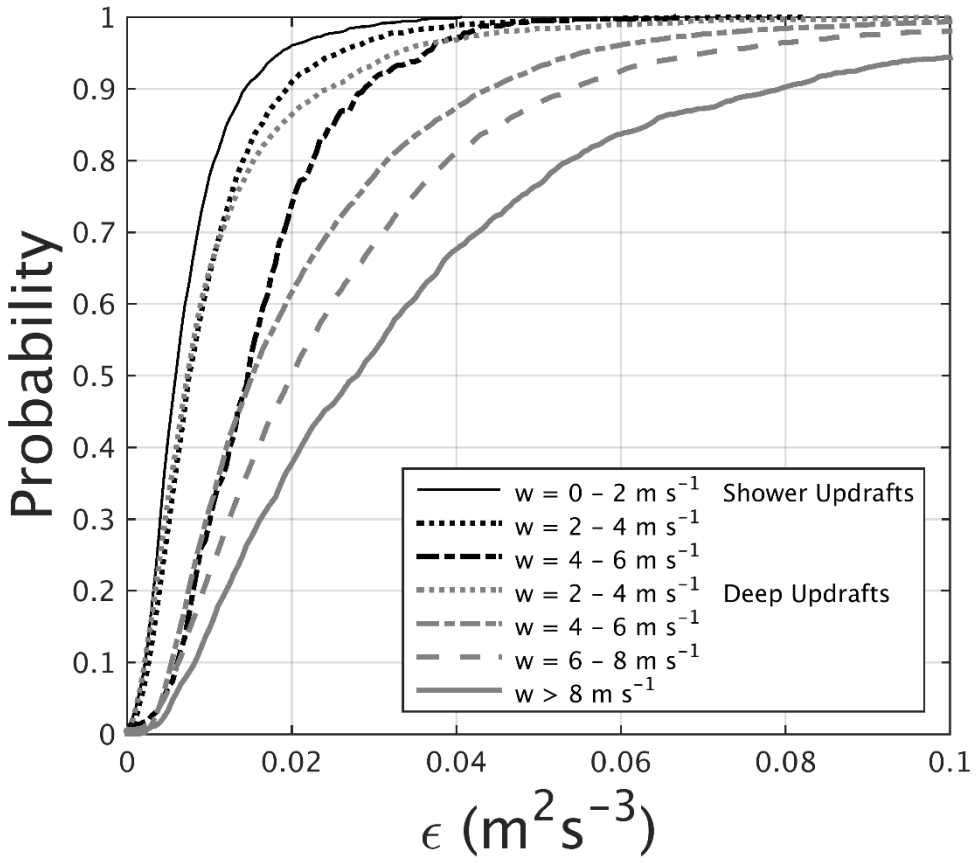
Probability
1
0.9
0.8
0.7
0.6
0.5
0.4
0.3
0.2
0.1
0
0
0.02
0.04
0.06
0.08
0.1
ϵ (m^{2}s^{-3})
w = 0 – 2 m s^{-1}
w = 2 – 4 m s^{-1}
w = 4 – 6 m s^{-1}
Shower Updrafts
w = 2 – 4 m s^{-1}
w = 4 – 6 m s^{-1}
w = 6 – 8 m s^{-1}
w > 8 m s^{-1}
Deep Updrafts

Figure 11